EES Catalysis

Accepted Manuscript

This article can be cited before page numbers have been issued, to do this please use: S. Wu, Q. Peng, C. Feng, H. Zhang, Z. Zhou, F. Dong and Z. Tang, *EES Catal.*, 2026, DOI: 10.1039/D6EY00068A.

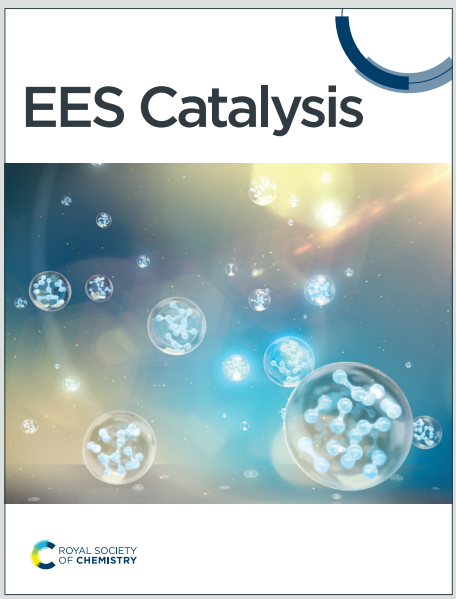

View Article Online
DOI: 10.1039/D6EY00068A

Broader context

Volatile organic compounds (VOCs), typified by propane, are key precursors of photochemical smog and tropospheric ozone, threatening the atmospheric environment and public health. Catalytic oxidation is the most effective industrial abatement route, yet state-of-the-art Co-based catalysts suffer severe deactivation under realistic flue gas conditions. The coexistence of H_2O and SO_2 causes competitive adsorption, active-site sulfidation, and irreversible degradation, restricting practical applications. Herein, we construct a layered-differentiated $Ni_1Co_{0.5}AlO_x$@Pt/ZSM-5 core-shell catalyst via supramolecular assembly and hydrothermal encapsulation. The Pt/ZSM-5 shell acts as a selective barrier to sequester H_2O and SO_2, while the LDH-derived core provides sufficient redox sites for propane activation. The optimized catalyst exhibits outstanding low-temperature activity, H_2O tolerance, and SO_2 durability. The core-shell interface optimizes electron transfer and stabilizes active species, reducing the C-H activation barrier. This work provides an atomic-level design principle for robust anti-poisoning catalysts toward efficient VOCs elimination in harsh industrial exhausts.

View Article Online
DOI: 10.1039/D6EY00068A

Engineering a layered-differentiation core-shell architecture: $NiCoAlO_x$@Pt/ZSM-5 for synergistically enhanced activity and dual H_2O/SO_2 resistance in propane oxidation

Shixing Wu[a, b#], Qian Peng[a, c#], Chao Feng[d], Haitao Zhang[e], Zhifang Zhou[*], Fang Dong[a*], Zhicheng Tang[a*]

(a. National Engineering Research Center for Fine Petrochemical Intermediates, State Key Laboratory of Low Carbon Catalysis and Carbon Dioxide Utilization, Lanzhou Institute of Chemical Physics, Chinese Academy of Sciences, Lanzhou 730000, China;

b. University of Chinese Academy of Sciences, Beijing 100039, China;

c. School of Metallurgy and Environment, Lanzhou University of Technology, Lanzhou 730050, China;

d. College of Chemical and Biological Engineering, Shandong University of Science and Technology, Qingdao, Shandong 266590, China;

e. Lanzhou Petrochemical Research Center, Petrochemical Research Institute, PetroChina, Lanzhou 730060, China.)

[#]These authors contributed equally: Shixing Wu, Qian Peng.

---

[*]Corresponding author.

E-mail address: zhouzf@lut.edu.cn (Z. Zhou), dongfang@licp.cas.cn (F. Dong), tangzhicheng@licp.cas.cn (Z. Tang).

View Article Online
DOI: 10.1039/D6EY00068A

Abstract:

Pt-based catalysts, though efficient for alkane C-H activation, suffer from water and SO_2 poisoning due to competitive adsorption on Pt sites. Herein, a core-shell $Ni_1Co_{0.5}AlO_x$@Pt/ZSM-5 catalyst was constructed via supramolecular assembly to improve its anti-poisoning performance, featuring a layered differentiation function. The ZSM-5 shell selectively sequesters H_2O and SO_2, preventing their access to Pt sites, while promoting the formation of active species such as Pt^0, Co^{3+}, and adsorbed oxygen. The optimized catalyst exhibits enhanced activity, water resistance, and sulfur tolerance in propane combustion. In situ DRIFTS confirmed the oxidation pathway as follows: propane is first activated at Pt^0 sites to form isopropyl species, subsequently oxidized via Co^{3+}-mediated sites to intermediates such as propene and acetate salts, and finally fully converted into CO_2 and H_2O with the participation of adsorbed oxygen. DFT calculations elucidated that this catalyst achieves superior propane oxidation activity and dual H_2O/SO_2 resistance via strengthened propane adsorption, reduced reaction energy barriers, and selective trapping of H_2O/SO_2 by the ZSM-5 shell. This atomic-level insight verifies that H_2O and SO_2 are preferentially sequestered by the ZSM-5 shell (rather than occupying Pt active sites), thus ensuring efficient propane/O_2 diffusion to Pt surfaces. This work provides a rational design strategy for robust, poisoning-resistant VOCs oxidation catalysts.

Keywords: Propane catalytic oxidation; H_2O/SO_2 anti-poisoning; Core-shell; LDH; ZSM-5.

View Article Online
DOI: 10.1039/D6EY00068A

1. Introduction

Volatile organic compounds (VOCs), primarily emitted from petrochemical, printing and dyeing, and manufacturing industries, are typically highly toxic, carcinogenic, and photochemically active, posing significant risks to both human health and the atmospheric environment.[1,2] Among various abatement strategies, catalytic combustion has emerged as one of the most effective technologies due to its high destruction efficiency, low ignition temperature, and minimal secondary pollution.[3-5] Propane (C_3H_8), a model VOCs, exhibits low reactivity at mild temperatures due to its strong C-H bonds. Accordingly, Pt-based catalysts are considered highly effective, owing to their superior C-H bond activation and oxygen adsorption/activation capabilities.[6,7] For Pt-based catalysts, the support exerts a critical influence on performance by regulating the dispersion and electronic structure of Pt species. As water vapor in industrial VOCs streams can deactivate catalysts through competitive adsorption or alteration of their physicochemical properties, hydrophobic supports effectively suppress water adsorption and enhance moisture tolerance.[8,9] Consequently, substantial research efforts have been devoted to the rational design of high-performance and durable catalysts capable of maintaining activity under complex and variable operating conditions.

Layered double hydroxides (LDHs), a class of anionic clays, have attracted considerable attention in heterogeneous catalysis due to their tunable composition and structure. Their general formula is $[M^{2+}_{1-x}M^{3+}_{x}(OH)_2]^{x+}(A^{n-})_{x/n}(mH_2O)$, where M^{2+} and M^{3+} represent divalent and trivalent metal cations (e.g., Ni^{2+}, Co^{2+}, Al^{3+}, Ce^{3+}), and A^{n-} and H_2O denote interlayer anions and water molecules, respectively.[10] Upon high-

View Article Online
DOI: 10.1039/D6EY00068A

temperature calcination, LDHs are converted into mixed metal oxides (MMOs) with mesoporous structures formed by stacked nanosheets, facilitating efficient reactant-active site interactions and product diffusion.[6,11,12] The presence of Al^{3+} promotes nanosheet growth, enhances crystallinity, and provides a robust framework for anchoring Ni and Co, thereby facilitating redox activity.[11] Furthermore, intercalation of anionic metal complexes such as $PtCl_6^{2-}$ into LDH interlayers enables the formation of atomically dispersed active sites upon calcination, driven by the two-dimensional (2D) confinement effect, thus enhancing catalytic stability.[13] For instance, Meng et al. synthesized a Ru_1Co_n single-atom alloy (SAA) catalyst by exploiting electrostatic repulsion between $RuCl_5^{2-}$ and interlayer anions, preventing agglomeration and enabling uniform dispersion during thermal treatment.[14] Similarly, Zhang et al. employed this strategy to prepare a highly active and stable Ru single-atom catalyst.[15] However, despite their excellent catalytic performance, LDH-derived oxides generally exhibit poor water resistance, likely due to the intrinsic hydrophilicity caused by Al species in the LDH precursor, highlighting the need to improve the moisture tolerance.[6, 11, 16]

Water vapor can significantly inhibit catalytic oxidation of VOCs by competitively occupying active sites or altering their physicochemical properties and this detrimental effect can be alleviated by employing hydrophobic coatings or supports, which reduce H_2O adsorption and minimize performance loss.[9] Coating the catalyst with appropriate shell materials not only protects the active metal from deactivation but also enables synergistic effects at the core-shell interface, thereby enhancing catalytic activity.[17]

View Article Online
DOI: 10.1039/D6EY00068A

ZSM-5, a silica-alumina zeolite with the general formula $M_{2/n}O \cdot Al_2O_3 \cdot ySiO_2 \cdot zH_2O$ (where n is the valence of the charge-compensating cation and y represents the SiO_2/Al_2O_3 ratio) features a unique ten-membered ring structure composed of interconnected SiO_4 or AlO_4 tetrahedra.[18] Its hydrophobicity is primarily governed by the SiO_2/Al_2O_3 ratio and the concentration of surface silanol groups.[19-22] Wang et al. showed that a higher SiO_2/Al_2O_3 ratio and lower Si-OH content in ZSM-5 confer greater hydrophobicity, which in turn enhances the water resistance of Pt/ZSM-5 catalysts.[20] Furthermore, researchers have conducted extensive studies on the sulfur resistance of catalytic oxidation systems for VOCs, with key strategies including hydrophobic zeolite coating, surface acidity regulation, core-shell spatial confinement, and modulation of metal electronic structures.[22] However, existing catalysts still generally suffer from difficulties in simultaneously resisting combined H_2O and SO_2 poisoning, the challenge of balancing activity and stability under complex atmospheres, and a lack of clarity regarding atomic-level anti-poisoning mechanisms. Very few studies have integrated the four key functions: propane activation, oxygen migration, resistance to H_2O poisoning, and resistance to SO_2 poisoning, into a single catalyst through the design of a layered core-shell structure.

To mitigate catalyst deactivation under H_2O/SO_2 exposure, a $Ni_1Co_{0.5}AlO_x$ catalyst derived from LDHs was synthesized via a supramolecular assembly strategy and hydrothermally coated with a Pt/ZSM-5 shell. Systematic modulation of Pt location (within $Ni_1Co_{0.5}AlO_x$ core or ZSM-5 shell) and shell thickness enabled performance optimization. The activity of $Ni_1Co_{0.5}AlO_x$@Pt/ZSM-5(3%) catalyst with Pt deposited

View Article Online
DOI: 10.1039/D6EY00068A

on the 3 wt% shell exhibits the optimal balance between H_2O and SO_2 resistance. The possible propane oxidation pathways under both air and SO_2-containing atmospheres were investigated by in-situ DRIFTS. This strategy offers a promising route to designing durable, high-performance Pt-based catalysts for propane oxidation under severe conditions.

2. Experimental

2.1. Synthesis of $Pt/Ni_aCo_bAlO_x$ catalysts

$Pt/Ni_aCo_bAlO_x$ catalysts were synthesized via a supramolecular assembly method, wherein NiAl-($PtCl_6^{2-}$)-LDH precursors were first prepared and subsequently calcined.[6, 15] The theoretical Pt loading and the molar ratio of (a+b)/c were fixed at 0.5 wt% and 3:1, respectively, while the Ni:Co molar ratio (a:b) was varied as 1:0, 1:0.5, 0.5:1, and 0:1. The synthesis procedures for other $Pt/Ni_aCo_bAlO_x$ catalysts followed the same synthetic route as that of $Pt/NiAlO_x$, with variations only in the amounts of $Ni(NO_3)_2{\cdot}6H_2O$, $Co(NO_3)_2{\cdot}6H_2O$ and H_2PtCl_4.

2.2. Synthesis of $Pt/Ni_1Co_{0.5}AlO_x$@ZSM-5(5%) catalyst

To systematically investigate the influence of Pt position on catalyst performance, we also prepared $Pt/Ni_1Co_{0.5}AlO_x$@ZSM-5(5%) catalyst. The $Pt/Ni_1Co_{0.5}AlO_x$ core was synthesized via the preparation of a $Ni_1Co_{0.5}Al$-($PtCl_6^{2-}$)-LDH precursor, following the same synthesis route as $Pt/Ni_1Co_{0.5}AlO_x$ catalyst. The resulting mixture was subjected to hydrothermal treatment at 180 °C for 48 h. Finally, the dried solid was ground into a uniform powder and calcined at 550 °C for 4 h (heating rate: 1 °C/min) to yield the $Pt/Ni_1Co_{0.5}AlO_x$@ZSM-5(5%) catalyst containing 0.5 wt% Pt.

View Article Online
DOI: 10.1039/D6EY00068A

2.3. Synthesis of $Ni_1Co_{0.5}AlO_x$@Pt/ZSM-5(3%), $Ni_1Co_{0.5}AlO_x$@Pt/ZSM-5(5%) and $Ni_1Co_{0.5}AlO_x$@Pt/ZSM-5(10%) catalysts

To systematically investigate the influence of shell content on the catalytic performance, core-shell catalysts with different shell thicknesses were also fabricated. The synthesis of Pt/ZSM-5 shells with varying mass fractions (3%, 5%, and 10%) followed the same procedure as the standard ZSM-5 shell synthesis, with modifications to the amounts of water glass, *n*-butylamine and replacement of the $Pt/Ni_1Co_{0.5}AlO_x$ core with corresponding amounts of $Ni_1Co_{0.5}AlO_x$ core. The detailed preparation procedure for catalysts with different Pt/ZSM-5 shell mass fractions is provided in the supporting information. The synthesis procedures of $Ni_1Co_{0.5}AlO_x$@Pt/ZSM-5 catalysts were illustrated in Fig. 1a.

2.4. Catalyst characterizations

Characterization techniques employed in this study included TEM, EDS mapping, XRD, Raman spectroscopy, FTIR, O_2/SO_2/H_2O/NH_3-TPD, H_2-TPR, BET surface area analysis, XPS, in-situ DRIFTS and DFT calculations. Detailed experimental procedures are provided in the supporting information.

2.5. Theoretical calculations

Density functional theory (DFT) calculations were performed using the Vienna ab-initio simulation package (VASP). Details concerning the definitions and computational procedures are provided in the supporting information.

3. Results and discussion

3.1. Morphology and microstructure

View Article Online
DOI: 10.1039/D6EY00068A

We observed the morphology of $Pt/Ni_1Co_{0.5}AlO_x$ and its core-shell catalysts via TEM electron microscopy, with results shown in Fig. 1, Fig. S1 and Fig. S2. The five catalysts retained well-defined nanosheet structures derived from the layered double hydroxide (LDH) precursors, confirming the successful synthesis of hydrotalcite-derived oxides. Compared with the $Pt/Ni_1Co_{0.5}AlO_x$ catalyst, the $Ni_1Co_{0.5}AlO_x$@Pt/ZSM-5 catalysts exhibited numerous disordered fibrous bundles of varying sizes distributed across the nanosheet surfaces (Fig. S1c-j). These straight, fiber-like structures contributed to the increased thickness of the nanosheets. Notably, the morphology and structure of the $Ni_1Co_{0.5}AlO_x$@Pt/ZSM-5(3%), $Ni_1Co_{0.5}AlO_x$@Pt/ZSM-5(5%), and $Ni_1Co_{0.5}AlO_x$@Pt/ZSM-5(10%) catalysts reveal that the thickness of the coating layer progressively increases with the rising Pt/ZSM-5 shell content (Fig. S1e, g and i). This indicates that ZSM-5 or Pt/ZSM-5 layers have successfully grown upon the surface of the LDH-derived oxides. The morphology and lattice spacing of the $Pt/Ni_1Co_{0.5}AlO_x$ catalyst are shown in Fig. 1b. The average particle size of $Pt/Ni_1Co_{0.5}AlO_x$ is approximately 33.18 nm, with a lattice spacing of 0.31 nm corresponding to the (220) plane of Co_3O_4. Fig. 1c displays the morphology and lattice spacing of the $Ni_1Co_{0.5}AlO_x$@Pt/ZSM-5(3%) sample. The average particle size of $Ni_1Co_{0.5}AlO_x$@Pt/ZSM-5(3%) is approximately 39.26 nm, slightly larger than that of $Pt/Ni_1Co_{0.5}AlO_x$, which indirectly confirms the successful encapsulation of the Pt/ZSM-5 shell. Elemental mapping of $Ni_1Co_{0.5}AlO_x$@Pt/ZSM-5(3%) catalyst in Fig. 1d reveals that Ni, Co, O, and Pt were homogeneously distributed within the nanosheet matrix, indicating uniform dispersion of active components, which is beneficial for

View Article Online
DOI: 10.1039/D6EY00068A

propane oxidation. The uniform distribution of Al provided abundant core sites for ZSM-5 or Pt/ZSM-5 shell growth, while the homogeneous dispersion of Si confirmed uniform coverage of the molecular sieve shells on the LDH-derived oxides.

3.2. Catalytic performance

Considering that the distribution of the active component Pt is a key factor influencing propane oxidation performance, we conducted a series of comparative performance tests on three catalysts: Pt/$Ni_1Co_{0.5}AlO_x$, Pt/$Ni_1Co_{0.5}AlO_x$@ZSM-5(5%), and $Ni_1Co_{0.5}AlO_x$@Pt/ZSM-5(5%). The results are presented in Fig. 2 and Fig. S3. Fig. 2 systematically investigates the influence of Pt distribution and ZSM-5 shell formation on the propane oxidation performance of Pt/$Ni_1Co_{0.5}AlO_x$-based catalysts. Under dry conditions, the Pt/$Ni_1Co_{0.5}AlO_x$ catalyst exhibits outstanding low-temperature catalytic activity, indicating that the active components are fully exposed and effectively promote propane oxidation (Fig. 2a). Upon introduction of 5 vol% H_2O, activity declined across all catalysts, with $Ni_1Co_{0.5}AlO_x$@Pt/ZSM-5(5%) exhibiting the smallest decrease, confirming the Pt/ZSM-5 shell structure's tolerance to water molecules (Fig. 2b). The Pt/$Ni_1Co_{0.5}AlO_x$@ZSM-5(5%) catalyst showed significantly improved water resistance (ΔT_{90} = -20 °C), although the encapsulated Pt was less accessible to propane, likely due to the overly thick ZSM-5 shell, resulting in a lower activity. Conversely, $Ni_1Co_{0.5}AlO_x$@Pt/ZSM-5(5%) retained high catalytic performance, demonstrating that water molecules did not significantly poison its active centers. This result confirms that confining Pt within the ZSM-5 shell constitutes an effective strategy. It maintains catalytic activity while suppressing water molecule

View Article Online
DOI: 10.1039/D6EY00068A

occupation of active sites, thereby mitigating activity decline. Fig. 2c and 2d calculate the apparent activation energies (E_a) for the three catalysts under dry and humid conditions. The E_a trends correlate closely with catalytic activity. Under water-permeable conditions, $Pt/Ni_1Co_{0.5}AlO_x$ exhibits a marked increase in E_a, indicating water molecules inhibit its low-temperature oxidation efficiency. Whereas $Ni_1Co_{0.5}AlO_x$@Pt/ZSM-5(5%) shows no discernible E_a shift, demonstrating that the ZSM-5 shell not only shields Pt active sites but also optimizes reactant diffusion and adsorption behavior, synergistically lowering the reaction energy barrier. Furthermore, we conducted water resistance stability tests on all three samples at T_{90} (temperatures corresponding to 90% propane conversion) under dry air conditions (Fig. 2e). After 20 h of reaction in a 5 vol% H_2O atmosphere, the propane conversion rate of $Ni_1Co_{0.5}AlO_x$@Pt/ZSM-5(5%) remained at 85.9%, substantially higher than the 55.9% observed for $Pt/Ni_1Co_{0.5}AlO_x$ without the shell. Similarly, the anti-SO_2 performance test results are shown in Fig. 2f. Under a 20 ppm SO_2 atmosphere, the $Pt/Ni_1Co_{0.5}AlO_x$ catalyst without the ZSM-5 shell exhibited a sharp decline in stability, ultimately achieving a conversion rate of only 42.2%. Whereas the $Ni_1Co_{0.5}AlO_x$@Pt/ZSM-5(5%) sample exhibited a gradual decrease in conversion rate. These findings demonstrate that the ZSM-5 shell physically shields active sites from contact with toxic molecules, preventing direct poisoning and significantly enhancing catalyst stability under complex atmospheres.

Based on the above performance analysis, we found that the percentage content of the Pt/ZSM-5 shell layer is crucial for enhancing the catalyst's resistance to poisoning

View Article Online
DOI: 10.1039/D6EY00068A

and stability. Therefore, we further prepared catalysts with varying Pt/ZSM-5 shell contents. Fig. 3 systematically investigates the influence of Pt/ZSM-5 shell content (3%, 5%, 10%) on the propane oxidation activity, kinetics, and poisoning resistance stability of the $Ni_1Co_{0.5}AlO_x$@Pt/ZSM-5 catalyst, identifying the optimal threshold effect of shell content. The results are illustrated in Fig. 3a-h, S4-10 and Table 1. Under dry air conditions, the propane oxidation activity followed the order: $Ni_1Co_{0.5}AlO_x$@Pt/ZSM-5(3%) > $Ni_1Co_{0.5}AlO_x$@Pt/ZSM-5(5%) > $Ni_1Co_{0.5}AlO_x$@Pt/ZSM-5(10%) (Fig. 3a). Compared to other core-shell catalysts, the enhanced activity of $Ni_1Co_{0.5}AlO_x$@Pt/ZSM-5(3%) probably arises from highly accessible Pt sites on the outer shell and a thin ZSM-5 layer that promotes efficient reactant diffusion. The introduction of 5% H_2O resulted in a slight decrease in activity for all catalysts. However, the 3% shell sample still exhibited the lowest T_{90} among the three, indicating that a lower shell layer content is more conducive to the diffusion and adsorption of reactants near the active sites (Fig. 3b). The $Ni_1Co_{0.5}AlO_x$@Pt/ZSM-5(3%) catalyst exhibits higher activity than the bare Pt/$Ni_1Co_{0.5}AlO_x$ catalyst under both dry air and 5 vol% H_2O conditions, indicating that the 3 wt% Pt/ZSM-5 shell enhances the redox performance and water tolerance of $Ni_1Co_{0.5}AlO_x$ core through interfacial interactions (Fig. S5).

To evaluate the practical applicability of these catalysts under realistic conditions, H_2O was introduced into the reaction feed to simulate typical industrial exhaust environments. As shown in Fig. 3c, under 5 vol% H_2O conditions, the propane conversions of the three catalysts remained stable during the initial 3 h but subsequently

View Article Online
DOI: 10.1039/D6EY00068A

declined by 16.2% ($Ni_1Co_{0.5}AlO_x$@Pt/ZSM-5(3%)), 4.57% ($Ni_1Co_{0.5}AlO_x$@Pt/ZSM-5(5%)) and 18.4% ($Ni_1Co_{0.5}AlO_x$@Pt/ZSM-5(10%)) over the next 12 h, respectively. This activity loss is likely due to competitive adsorption of H_2O molecules with propane, O_2, and reactive intermediates on active sites, which weakens reactant adsorption and inhibits the formation of reactive species. Consequently, the interaction between reactants and active centers is suppressed, leading to reduced catalytic activity. Furthermore, H_2O may irreversibly deactivate moisture-sensitive active sites through direct interaction, resulting in permanent loss of activity. Compared to the Pt/$Ni_1Co_{0.5}AlO_x$ catalyst, the four core-shell catalysts exhibited reduced activity loss, indicating that the ZSM-5 shell effectively suppressed H_2O adsorption and inhibited direct interaction between H_2O and active sites. An increased H_2O resistance of the four core-shell catalysts may stem from the relatively high Si/Al ratio of ZSM-5, which reduces the density of polar Si-O-Al linkages while increasing nonpolar Si-O-Si bonds, thereby weakening the interaction between polar H_2O molecules and active sites and decreasing hydrophilicity.[19] Additionally, the optimal anti-H_2O stability of $Ni_1Co_{0.5}AlO_x$@Pt/ZSM-5(5%) catalyst may arise from its moderately thick hydrophobic Pt/ZSM-5 shell, which potentially inhibits H_2O adsorption and shields Pt from water-sensitive sites in LDH-derived $Ni_1Co_{0.5}AlO_x$ core. To determine the E_a under dry air and 5 vol% H_2O conditions, four data points with propane conversion below 20% were selected from the activity curves in Fig. 3a and b. The corresponding E_a are summarized in Fig. 3d, e and Table 1. Generally, a lower E_a indicates that VOCs molecules are more readily activated on the catalyst surface, reflecting higher intrinsic

View Article Online
DOI: 10.1039/D6EY00068A

activity. Under dry conditions, E_a followed the trend: $Ni_1Co_{0.5}AlO_x$@Pt/ZSM-5(3%) < $Ni_1Co_{0.5}AlO_x$@Pt/ZSM-5(5%) < $Ni_1Co_{0.5}AlO_x$@Pt/ZSM-5(10%), which is consistent with their activity ranking, confirming differences in ease of propane activation over different catalyst surfaces. As shown in Fig. S6, E_a, reaction rate (r) and T_{90} of the same catalyst exhibit strong linear correlations, with E_a and r showing inverse trends relative to T_{90}, indicating that lower activation energy and higher reaction rates correspond to enhanced catalytic activity.

Catalytic stability tests of Pt/$Ni_1Co_{0.5}AlO_x$ and its core-shell catalysts were performed at constant temperatures corresponding to high propane conversions (85.0-95.0%), with SO_2 introduced as needed. The SO_2 tolerance of the catalysts was also evaluated, as shown in Fig. 3f. After 12 h exposure to SO_2, propane conversion over Pt/$Ni_1Co_{0.5}AlO_x$ catalyst dropped sharply by 44.9% and did not recover after SO_2 removal, suggesting severe and irreversible SO_2 poisoning. In contrast, the decreases of propane conversion for Pt/$Ni_1Co_{0.5}AlO_x$@ZSM-5(5%), $Ni_1Co_{0.5}AlO_x$@Pt/ZSM-5(5%), and $Ni_1Co_{0.5}AlO_x$@Pt/ZSM-5(10%) catalysts were less distinct, while $Ni_1Co_{0.5}AlO_x$@Pt/ZSM-5(3%) catalyst even showed a 4.66% increase. The temporary increase in propane conversion on $Ni_1Co_{0.5}AlO_x$@Pt/ZSM-5(3%) catalyst during SO_2 exposure may be attributed to the formation of sulfate/sulfite species with strong Lewis acidity, which promote propane adsorption and C-H bond activation.[23] These results demonstrate $Ni_1Co_{0.5}AlO_x$@Pt/ZSM-5(3%) catalyst's excellent SO_2 tolerance and highlight its strong potential for practical applications.[24] However, once SO_2 was removed, the five catalysts exhibited greater decreases in activity, likely due to the

View Article Online
DOI: 10.1039/D6EY00068A

irreversible deactivation of active sites. As shown in Fig. S10, after 20 h of propane oxidation under dry conditions, the propane conversion over $Pt/Ni_1Co_{0.5}AlO_x$ catalyst declined by 8.20%, whereas the decrease for the four core-shell catalysts remained below 5.00%, indicating that the ZSM-5 and Pt/ZSM-5 shell effectively enhanced the thermal stability of the hydrotalcite-derived catalysts.

To further evaluate catalytic efficiency, the reaction rates normalized by specific surface area (R_s) and catalyst mass (R_m) were calculated at 140, 160, 180, 200, and 220 ^oC under both dry air and 5 vol% H_2O conditions, as shown in Fig. 3g and S7. The $Ni_1Co_{0.5}AlO_x$@Pt/ZSM-5(3%) catalyst exhibited the highest R_s and R_m at every temperature point, which were 4.3-7.6 and 2.6-6.2 times greater than those of other catalysts, respectively, indicating the highest catalytic efficiency. Furthermore, $Ni_1Co_{0.5}AlO_x$@Pt/ZSM-5(3%) catalyst showed the smallest decrease in R_s and R_m under 5 vol% H_2O conditions, confirming its superior activity and water resistance. Turnover frequencies (TOF) based on the active metals under dry air and 5 vol% H_2O conditions were also calculated. Under dry conditions, the TOF_{Pt} at 220 ^oC confirming that the interactions between the 3 wt% Pt/ZSM-5 shell and $Ni_1Co_{0.5}AlO_x$ core enhance the intrinsic oxidation activity of $Ni_1Co_{0.5}AlO_x$@Pt/ZSM-5(3%) catalyst. In contrast, all catalysts exhibited lower TOF_{Pt}, TOF_{Ni} and TOF_{Co} under 5 vol% H_2O conditions, highlighting the inhibitory effect of water vapor on the intrinsic reaction kinetics (Fig. S8). Fig. S9 shows the good linear correlations between TOF_{Pt} and T_{90} of the catalyst under both dry air and 5 vol% H_2O conditions, suggesting that intrinsic catalytic activity directly governs light-off performance.

View Article Online
DOI: 10.1039/D6EY00068A

As shown in Fig. 3h, the CO_2 selectivity trend highly correlates with the propane conversion rate trend, confirming the high catalytic efficiency of $Pt/Ni_1Co_{0.5}AlO_x$ and its core-shell catalysts. The $Ni_1Co_{0.5}AlO_x$@Pt/ZSM-5(3%) catalyst exhibits outstanding CO_2 selectivity, rising rapidly in the ~200 °C and approaching 100% in the medium-to-high temperature range (>300 °C), consistently remaining significantly higher than other catalysts. The $Ni_1Co_{0.5}AlO_x$@Pt/ZSM-5(3%) catalyst not only efficiently activates propane at low temperatures but also drives the oxidation reaction to a deeper extent, significantly suppressing the formation of intermediate products. To provide an intuitive comparison of the propane catalytic combustion activity among different Pt-based catalysts, Fig. 3i and Table 2 present an analysis centered on T_{50} and T_{90} as core metrics. Notably, the T_{50} and T_{90} values of the $Ni_1Co_{0.5}AlO_x$@Pt/ZSM-5(3%) catalyst prepared in this work are significantly lower than those of conventional Pt-based catalysts, directly demonstrating its outstanding low-temperature activity advantage in propane catalytic combustion. Conventional Pt-based catalysts generally exhibit elevated T_{50} and T_{90} values due to weak interactions between the support and Pt, coupled with insufficient adsorption and activation capabilities for propane. The $Ni_1Co_{0.5}AlO_x$@Pt/ZSM-5(3%) catalyst overcomes this limitation through core-shell synergistic effects. ZSM-5 not only stabilizes Pt nanoparticles via strong interactions but also provides abundant oxygen vacancies and active oxygen species, thereby enhancing the low-temperature activation of propane C-H bonds.

3.3. Physicochemical properties of catalysts

The pore properties of $Pt/Ni_1Co_{0.5}AlO_x$ and its core-shell catalysts are depicted in

View Article Online
DOI: 10.1039/D6EY00068A

Fig. 4a and b. Both $Pt/Ni_1Co_{0.5}AlO_x$ and $Ni_1Co_{0.5}AlO_x$@Pt/ZSM-5(3%) catalysts exhibited type IV isotherms based on the IUPAC classification, characteristic of mesoporous materials.[25] The $Pt/Ni_1Co_{0.5}AlO_x$ catalyst displayed an H2 hysteresis loop, typically associated with ink-bottle-shaped pores, which likely originated from the partial collapse of LDH structure during calcination at 400 °C.[26] In contrast, $Ni_1Co_{0.5}AlO_x$@Pt/ZSM-5(3%) catalyst showed an H3 hysteresis loop, indicative of slit-shaped pores formed by the stacking of lamellar nanosheets. This suggests that the thin Pt/ZSM-5 coating preserved the mesostructural features of LDH-derived oxide.[27] In accordance with the literature, the unique micro-mesoporous composite structure may provide more optimal pathways for the adsorption and diffusion of propane.[28-30] As shown in Fig. 4b and Table S1, the five catalysts exhibited broad pore size distributions with abundant mesopores and relatively large specific surface areas, offering numerous contact sites for propane adsorption and oxidation. Compared with the $Pt/Ni_1Co_{0.5}AlO_x$ catalyst, the four coated catalysts displayed slightly reduced mesopore volumes and surface areas in Table S1, likely due to partial pore coverage by the ZSM-5 or Pt/ZSM-5 shell.

The crystalline phase structures of $Pt/Ni_1Co_{0.5}AlO_x$ and its core-shell catalysts were examined by XRD technology, as depicted in Fig. 4c and S11. All five catalysts exhibited diffraction peaks at 19.1°, 31.4°, 37.0° and 45.0°, assigned to the (111), (220), (311), and (400) planes of $NiAl_2O_4$ (JCPDS 78-0052) and NiO (JCPDS 71-1179), as well as peaks at 19.0°, 31.3°, 36.8°, 44.8°, 59.4° and 65.2° attributed to (111), (220), (311), (400), (511) and (440) of Co_3O_4 (JCPDS 74-2120), respectively.[24,31] The absence

View Article Online
DOI: 10.1039/D6EY00068A

of characteristic peaks for Al_2O_3 suggests that Al may be incorporated into $NiAl_2O_4$ spinel structures, existing as amorphous phases, or being integrated into the ZSM-5 framework.[32] The observed Ni-based and Co-based oxide peaks confirm the successful formation of mixed metal oxides derived from the hydrotalcite precursor. These peaks appeared slightly weakened in the four core-shell catalysts, likely due to the shielding effect of the ZSM-5 and Pt/ZSM-5 shells. No distinct diffraction peaks corresponding to ZSM-5 were detected, which may be attributed to the low crystallinity.[33] Similarly, the absence of Pt-related reflections indicates that Pt species may be highly dispersed in LDH derivatives and ZSM-5 due to the 2D space confinement effect of hydrotalcite or interaction between Pt and ZSM-5.[14,34]

To gain deeper insight into the electronic interactions and structural evolution mechanisms induced by the core-shell structure, this study conducted localized electron function (ELF) calculations and structural optimization. The relevant results are shown in Fig. 4d (A1-A4). The ELF distribution maps (A1 for $Pt/Ni_1Co_{0.5}AlO_x$ and A2 for $Ni_1Co_{0.5}AlO_x$@Pt/ZSM-5) visually represent the spatial distribution of electron localization, directly reflecting the chemical bonding nature and electron transfer characteristics at the interface. In A1 ($Pt/Ni_1Co_{0.5}AlO_x$), the electron localization around Pt atoms and Ni/Co sites exhibits a relatively uniform distribution, indicating the formation of metallic or ionic bonds within the LDH-derived oxide. Conversely, A2 ($Ni_1Co_{0.5}AlO_x$@Pt/ZSM-5) exhibits distinct electron localization patterns: the introduction of the ZSM-5 shell induces redistribution of electron density at the core-shell interface, enhancing electron localization around Si-O-Pt and Si-O-Co bonds. This

View Article Online
DOI: 10.1039/D6EY00068A

interface-driven electronic rearrangement aligns with XPS findings, wherein the core-shell architecture modulates the oxidation states of Pt. Specifically, electron delocalization at the Pt/ZSM-5 interface promotes the formation of Pt^{4+} species, which exhibit reduced reactivity towards SO_2 and H_2O (verified by DFT adsorption energy calculations), thereby conferring exceptional anti-poisoning properties to the catalyst. Optimized structural models (A3: $Pt/Ni_1Co_{0.5}AlO_x$; A4: $Ni_1Co_{0.5}AlO_x$@Pt/ZSM-5) further elucidate the geometric and electronic effects of the core-shell design. In A3 ($Pt/Ni_1Co_{0.5}AlO_x$), Pt atoms are embedded within the $NiCoAlO_x$, forming a relatively compact structure with limited exposure of Pt active sites. In contrast, the A4 model ($Ni_1Co_{0.5}AlO_x$@Pt/ZSM-5) shows Pt atoms anchored to the ZSM-5 surface, whose porous framework not only stabilizes Pt nanoparticles but also creates accessible pathways for propane/O_2 diffusion. Furthermore, the Si-O-Pt bonds in the A4 model induce tensile strain in the platinum atoms. Prior studies indicate that such strain enhances C-H bond adsorption and activation. Collectively, these theoretical findings provide atomic-level evidence for core-shell synergy. The ZSM-5 shell modulates interfacial electron distribution through electronic free energy redistribution, while structural engineering optimizes the geometric environment of Pt active sites, thereby simultaneously enhancing catalytic activity and resistance to poisoning.

The phase structure evolution of $Pt/Ni_1Co_{0.5}AlO_x$ and its core-shell catalysts was investigated via Raman spectroscopy, as shown in Fig. 4e. A prominent Raman band at 543 cm^{-1}, close to the characteristic peak of NiO (540 cm^{-1}), suggests the incorporation of Al^{3+} into the NiO lattice, forming Ni-O-Al bonds. This observation aligns with the

View Article Online
DOI: 10.1039/D6EY00068A

absence of Al_2O_3-related peaks, supporting the inference that Al is integrated into the Ni-based oxide and ZSM-5 framework rather than existing as a separate phase.[6,24] The faint Raman peak at 588 cm^{-1} of the five catalysts is attributed to the $NiAl_2O_4$ spinel phase, and the lack of additional spinel-related peaks is likely due to structural disorder induced by the insertion of Al into NiO lattices, which disrupts long-range order and diminishes peak visibility.[35] In the four coated catalysts, broad and weak bands observed in the 600-700 cm^{-1} and 800-1000 cm^{-1} regions correspond to the bending and stretching vibrations of T-O-T and T-O (T = Si, Al) bonds, respectively, indicating the presence of ZSM-5 or Pt/ZSM-5 frameworks.[29] The Si-O-Si bond in ZSM-5 framework is a nonpolar species and shows weak affinity to polar water molecules, thus imparting good water resistance to the four coated catalysts in this work.[19]

The functional groups of $Pt/Ni_1Co_{0.5}AlO_x$ and $Ni_1Co_{0.5}AlO_x$@Pt/ZSM-5(3%) catalysts were investigated via FTIR spectroscopy, as shown in Fig. 4f. Both catalysts exhibit characteristic bands at 3435 and 1630 cm^{-1}, corresponding to surface hydroxyl groups and physically adsorbed water (O-H and H-O-H vibrations), along with a band at 2922 cm^{-1} attributed to C-H stretching and a peak at 1385 cm^{-1} arising from C-O vibrations of carbonate species.[36,37] The broad band between 400-510 cm^{-1} is associated with M-O (M = Ni, Co, Al) lattice vibrations, confirming the formation of mixed metal oxides derived from hydrotalcite precursors.[37,38] The Si-O-Si bond in the framework imparts ZSM-5 hydrophobicity, thus improving the water resistance of $Ni_1Co_{0.5}AlO_x$@Pt/ZSM-5(3%) catalyst.[19] Furthermore, the markedly reduced intensity of O-H related bands (3435 and 1630 cm^{-1}) in $Ni_1Co_{0.5}AlO_x$@Pt/ZSM-5(3%) catalyst

View Article Online
DOI: 10.1039/D6EY00068A

suggests enhanced surface hydrophobicity imparted by the zeolite layer. These spectral features collectively confirm the core-shell structure and demonstrate that the Pt/ZSM-5 shell alters the surface environment, potentially contributing to improved hydrothermal resistance and catalytic performance.

XPS analysis was performed on Pt/$Ni_1Co_{0.5}AlO_x$ and its core-shell catalysts, and the corresponding spectra are presented in Fig. 5a-e, S12 and S13. Due to the overlap between Pt 4f and Al 2p/Ni 3p signals, the Pt 4f spectra were fitted by fixing the Pt $4f_{7/2}$ to Pt $4f_{5/2}$ intensity ratio at 4:3 and maintaining a binding energy separation of 3.3 eV, as shown in Fig. 5a. Peaks at 67.60-67.86 eV and 69.60-69.86 eV were assigned to Ni 3p, while the signal at 74.00 eV corresponded to Al 2p.[27] In the Pt 4f region, the peaks at 71.40 and 74.70 eV were attributed to metallic Pt^0, those at 72.50 and 75.80 eV to Pt^{2+}, and those at 74.20 and 77.50 eV to Pt^{4+} species.[7] The dominance of metallic Pt^0 species on the five catalysts suggests the successful deposition of Pt nanoparticles on the $Ni_1Co_{0.5}AlO_x$ core and ZSM-5 shell. Among these catalysts, $Ni_1Co_{0.5}AlO_x$@Pt/ZSM-5(3%) and Pt/$Ni_1Co_{0.5}AlO_x$ exhibited the highest proportions of Pt^0, which facilitates O_2 activation and C-H bond cleavage, thereby resulting in superior catalytic activity. However, the exposed Pt^0 sites on Pt/$Ni_1Co_{0.5}AlO_x$ catalyst are susceptible to oxidation by SO_2 and competitive adsorption by H_2O, resulting in poor resistance to sulfur and moisture.[9,39] Conversely, the catalysts coated with ZSM-5 and Pt/ZSM-5 exhibited higher Pt^{4+} content, illustrating that interactions between Pt and ZSM-5 promote the formation of high-valence Pt species, which is likely due to stabilization by the oxygen-rich environment and Al sites within the ZSM-5 shell.[40] Pt^{4+}

View Article Online
DOI: 10.1039/D6EY00068A

offers superior chemical stability and lower reactivity toward SO_2 and H_2O, improving catalyst durability under harsh conditions.[41] Moreover, the hydrophobic ZSM-5 shell acts as a physical barrier that suppresses SO_2 and H_2O access to Pt^0 sites, thereby enhancing the poison resistance of the four core-shell catalysts. Additionally, this protective effect is more prominent with increased shell thickness or embedded Pt configurations. For instance, as shown in Fig. 3c, the $Ni_1Co_{0.5}AlO_x$@Pt/ZSM-5(5%) catalyst, featuring a 5 wt% ZSM-5 shell with embedded Pt, exhibits superior water resistance compared to both the $Ni_1Co_{0.5}AlO_x$@Pt/ZSM-5(3%) catalyst with a thinner (3 wt%) shell and Pt/$Ni_1Co_{0.5}AlO_x$@ZSM-5(5%) catalyst, where Pt is confined into the $Ni_1Co_{0.5}AlO_x$ core.

As shown in Fig. 5b, the O 1s XPS spectra of Pt/$Ni_1Co_{0.5}AlO_x$ and its core-shell catalysts exhibit three distinct peaks. The peak at 530.35-530.60 eV corresponds to lattice oxygen (O_{latt}), while those at 531.42-531.78 eV and 532.52-532.98 eV are attributed to adsorbed oxygen (O_{ads}) and surface hydroxyl groups (O_{wat}), respectively.[42] Compared with the bare Pt/$Ni_1Co_{0.5}AlO_x$ catalyst, the four coated catalysts exhibit positive shifts in the O_{latt} binding energy and increased proportions of O_{latt} (Fig. S12a). This enhancement is likely due to the oxidizing environment provided by Al and O species in the ZSM-5 shell, which strengthens M-O bonds and stabilizes high-valence metal cations, thereby promoting tolerance to SO_2 and H_2O.[40] The increase of O_{latt} content is particularly advantageous under humid and sulfur-rich conditions, where lattice oxygen plays a compensatory role when surface active oxygen is poisoned, thereby enhancing catalyst durability and poison resistance.[43] Furthermore, the four

View Article Online
DOI: 10.1039/D6EY00068A

coated catalysts show positive shifts in the O_{ads} BE values compared to the bare $Pt/Ni_1Co_{0.5}AlO_x$ catalyst, indicating that strong adsorption likely prevents rapid loss of active oxygen under SO_2- or H_2O-containing conditions. Meanwhile, after being coated with ZSM-5 or Pt/ZSM-5 shell, the O_{ads} content in the catalysts decreases, except for $Ni_1Co_{0.5}AlO_x$@Pt/ZSM-5(5%) and $Ni_1Co_{0.5}AlO_x$@Pt/ZSM-5(3%). As a more reactive and mobile species, O_{ads} is crucial for low-temperature oxidation and often associated with oxygen vacancies.[6,44,45] The higher O_{ads} content in $Ni_1Co_{0.5}AlO_x$@Pt/ZSM-5(3%) catalyst aligns with its superior activity, while the lower O_{ads} levels in other coated samples are consistent with reduced activity, highlighting the essential role of adsorbed oxygen in catalytic efficiency.

As shown in Fig. 5c, the Ni 2p XPS spectra of $Pt/Ni_1Co_{0.5}AlO_x$ and its core-shell catalysts display two main peaks in the Ni $2p_{3/2}$ region at 855.80 and 857.52 eV, corresponding to Ni^{2+} and Ni^{3+} species, respectively, along with a satellite feature near 862 eV. Similarly, in the Ni $2p_{1/2}$ region, peaks at 873.80 and 875.52 eV were assigned to Ni^{2+} and Ni^{3+}, with a satellite peak around 880 eV.[24,27] Compared with bare $Pt/Ni_1Co_{0.5}AlO_x$ catalyst, the four coated catalysts exhibit increased Ni^{3+}/Ni^{2+} ratios, while the Ni 2p binding energies remain essentially unchanged. This indicates that ZSM-5 coating promotes Ni oxidation without altering its local coordination environment, indicative of surface reconstruction induced by the interactions between $Ni_1Co_{0.5}AlO_x$ core and P/ZSM-5 shell. As shown in Fig. 5d, the deconvoluted Co 2p XPS spectra reveal Co^{3+} peaks at 780.70-780.98 eV and 795.70-795.98 eV, and Co^{2+} peaks at 782.77-783.15 eV and 797.77-798.15 eV.[24] As shown in Fig. 5d and S12b,

View Article Online
DOI: 10.1039/D6EY00068A

compared to bare $Pt/Ni_1Co_{0.5}AlO_x$, the four coated catalysts exhibit positive shifts in Co^{3+} binding energies and a marked increase in Co^{3+} content, indicating that ZSM-5 favors the stabilization of high-valence cobalt species by interactions between core and shell. As Co^{3+} facilitates oxygen mobility and redox cycling, its highest proportion in $Ni_1Co_{0.5}AlO_x$@Pt/ZSM-5(3%) catalyst correlates with the best low-temperature activity, highlighting the critical role of a high Co^{3+}/Co^{2+} ratio in catalytic efficiency.[24] The XPS spectrum of Si 2p is shown in Fig. S13.

Fig. 5e and Fig. S14 reveal clear negative correlations between ΔT_{90} and the contents of Pt^{4+}, O_{latt} and $Si_{framework}$ (framework Si species), with $Si_{framework}$ in $Pt/Ni_1Co_{0.5}AlO_x$@ZSM-5(5%) catalyst exhibiting an exceptionally strong inverse relationship. It demonstrates that Pt^{4+}, O_{latt} and $Si_{framework}$ enhance water tolerance by offering lower reactivity toward H_2O, compensatory oxygen species under humid conditions, and hydrophobicity to prevent competitive adsorption of H_2O, respectively. The core-shell catalyst contains higher concentrations of high-valence metal ions such as Co^{3+} and Pt^{4+} compared to the bare $Pt/Ni_1Co_{0.5}AlO_x$ catalyst, confirming that the core-shell interactions promote the formation and stabilization of these oxidized species.

The reducibility of $Pt/Ni_1Co_{0.5}AlO_x$ and its core-shell catalysts was investigated via H_2-TPR characterization, as presented in Fig. 5f, g and S15. Typically, Pt species reduce in the 60-120 ^oC range, but the corresponding signals were too weak to be resolved, likely due to the limited interaction between Pt and $Ni_1Co_{0.5}AlO_x$.[46,47] The bare $Pt/Ni_1Co_{0.5}AlO_x$ catalyst exhibits a sharp peak at 300 ^oC and a strongly broad peak

View Article Online
DOI: 10.1039/D6EY00068A

around 460 °C corresponding to the transition of NiO → Ni^0 and Co_3O_4 → CoO → Co^0, respectively, and a weakly broad peak at ~750 °C corresponding to the overall reduction of $NiAl_2O_4$ spinel phase.[47-53] This enhanced reducibility might partly account for the optimal activity of $Ni_1Co_{0.5}AlO_x$@Pt/ZSM-5(3%) catalyst compared to the bare Pt/$Ni_1Co_{0.5}AlO_x$ catalyst.

The acidity properties of the Pt/$Ni_1Co_{0.5}AlO_x$ and its core-shell catalysts were evaluated by NH_3-TPD, as exhibited in Fig. 5h and S16a. The profiles exhibit three distinct desorption regions corresponding to weak (50-300 °C), medium-strong (300-500 °C), and strong (500-800 °C) acid sites.[4] Compared to bare Pt/$Ni_1Co_{0.5}AlO_x$ catalyst, the four core-shell catalysts show increased proportions of weak and medium-strong acid sites after coating with ZSM-5 and Pt/ZSM-5, enhancing propane adsorption and activation.[54-57] Specifically, the total percentage of weak and medium-strong acid sites follows the trend: Pt/$Ni_1Co_{0.5}AlO_x$ (70.3%) < $Ni_1Co_{0.5}AlO_x$@Pt/ZSM-5(5%) (76.0%) < $Ni_1Co_{0.5}AlO_x$@Pt/ZSM-5(10%) (77.9%) < Pt/$Ni_1Co_{0.5}AlO_x$@ZSM-5(5%) (78.8%) < $Ni_1Co_{0.5}AlO_x$@Pt/ZSM-5(3%) (80.1%), with the highest value in $Ni_1Co_{0.5}AlO_x$@Pt/ZSM-5(3%) catalyst correlating with its optimal catalytic activity. These acid sites include both Brønsted and Lewis types: Brønsted sites originate from surface hydroxyl groups (Ni-OH, Co-OH and Al-OH) in $Ni_1Co_{0.5}AlO_x$ and bridging Si-OH-Al in the ZSM-5 framework, while Lewis sites arise from coordinatively unsaturated metal centers and extra-framework species. Their synergistic roles enhance propane adsorption, C-H bond cleavage, and oxidation efficiency, promoting propane consumption.[58,59] Moreover, Fig. S16a shows that the amount of acid sites on the four

View Article Online
DOI: 10.1039/D6EY00068A

coated catalysts remains unchanged compared to $Pt/Ni_1Co_{0.5}AlO_x$ catalyst, which likely favors the dominance of metallic Pt^0, partly accounting for the optimal activity of $Ni_1Co_{0.5}AlO_x$@Pt/ZSM-5(3%) catalyst.[60]

The oxygen species of the $Pt/Ni_1Co_{0.5}AlO_x$ and its core-shell catalysts were investigated by O_2-TPD, as depicted in Fig. 5i and S16b. The O_2-TPD profiles can be categorized into adsorbed oxygen (O_α) (50-300 °C), surface lattice oxygen (O_β) (300-600 °C), and bulk lattice oxygen (O_γ) (600-900 °C).[57] The relative content of O_α decreased in the order: $Pt/Ni_1Co_{0.5}AlO_x$@ZSM-5(5%) (20.7%) > $Ni_1Co_{0.5}AlO_x$@Pt/ZSM-5(3%) (17.1%) > $Pt/Ni_1Co_{0.5}AlO_x$ (16.7%) > $Ni_1Co_{0.5}AlO_x$@Pt/ZSM-5(5%) (14.1%) > $Ni_1Co_{0.5}AlO_x$@Pt/ZSM-5(10%) (11.2%). This trend suggests that the movement of Pt species from $Ni_1Co_{0.5}AlO_x$ core to ZSM-5 shell and increased shell thickness suppresses the formation of reactive adsorbed oxygen, leading to reduced low-temperature activity. As O_α and O_β are the primary active oxygen species, their depletion in $Pt/Ni_1Co_{0.5}AlO_x$@Z(5%), $Ni_1Co_{0.5}AlO_x$@Pt/ZSM-5(5%), and $Ni_1Co_{0.5}AlO_x$@Pt/ZSM-5(10%) catalysts may be responsible for the decline in catalytic activity.[61] In contrast, coating with ZSM-5 and Pt/ZSM-5 significantly increased the amount of O_γ, likely due to enhanced bulk oxygen storage and release at elevated temperatures, which improved high-temperature oxygen cycling and contributed to better hydrothermal stability.[43] Additionally, Fig. S16b reveals that the four coated catalysts have less amount of oxygen species than the $Pt/Ni_1Co_{0.5}AlO_x$ catalyst, indicating that the core-shell interactions modified oxygen species of hydrotalcite-derived oxides. Overall, ZSM-5-based shell coatings markedly

View Article Online
DOI: 10.1039/D6EY00068A

altered the oxygen species distribution, thereby influencing catalytic activity and durability.

4. Exploration and discussion about the resistant poison mechanism of ZSM-5 shell

To elucidate the reaction behaviors of propane over the $Ni_1Co_{0.5}AlO_x$@Pt/ZSM-5(3%) catalyst under both air and SO_2-containing atmospheres, in-situ DRIFTS experiments were conducted to investigate its adsorption and oxidation behavior, as shown in Fig. 6 and S17. For the air atmosphere, $Ni_1Co_{0.5}AlO_x$@Pt/ZSM-5(3%) catalyst was first pretreated in N_2 at 400 °C for 30 min and then cooled to 40 °C. A C_3H_8/Ar gas mixture containing 2000 ppm propane was subsequently introduced until surface saturation was reached. After purging with N_2 to remove weakly adsorbed species, the gas was switched to 20% O_2/N_2 mixture, and spectra were recorded during stepwise heating (100 °C, 150 °C, 200 °C, 250 °C, 300 °C, and 350 °C) to monitor surface species evolution. Fig. 6a and b present the in-situ DRIFTS spectra of propane adsorption at 40 °C. After 6 min of propane exposure, characteristic asymmetric stretching bands of -CH_3 and -CH_2- groups appeared at 2970, 2892, and 2865 cm^{-1}, indicating initial propane adsorption.[4,7] By 8 min, these bands intensified, and new peaks emerged at 1474 cm^{-1} (-CH_2- bending), 1373 cm^{-1} (-CH_3 bending), and 1451 and 1541 cm^{-1} (COO^- stretching), associated with carboxylate species.[7,62] These observations suggest that propane undergoes partial oxidation by surface oxygen species, even in the absence of gaseous O_2.[7,57] The continued increase in peak intensity until 26 min reflects progressive surface accumulation of propane, leading to saturation.

View Article Online
DOI: 10.1039/D6EY00068A

Fig. 6b-d depict the stepwise oxidation of propane over $Ni_1Co_{0.5}AlO_x$@Pt/ZSM-5(3%) catalyst under an air atmosphere. As the temperature rises, the characteristic C-H stretching bands of -CH_3 and -CH_2- groups (2800-3100 cm^{-1}) diminish and evolve into negative peaks by 100 °C, indicating the consumption of pre-adsorbed propane. Simultaneously, new weak bands emerge in the 1200-1800 cm^{-1} region, corresponding to oxidation intermediates. Specifically, peaks at 1640 cm^{-1} (C=C), 1697 cm^{-1} (C=O), and 1724 cm^{-1} (C=O) are assigned to propylene, acetone, and propionaldehyde species, respectively.[4,7,62] Bands at 1610 cm^{-1} and 1352 cm^{-1} correspond to formate species ($HCOO^-$), while those at 1582 cm^{-1} and 1468 cm^{-1} are attributed to acetate species (CH_3COO^-).[57,63] These intermediates exhibit a temperature-dependent behavior: initially increasing in intensity and then diminishing, suggesting their transient formation and further oxidation. In parallel, bands at 1550 cm^{-1} and 1530 cm^{-1} are associated with carbonate species (CO_3^{2-}), while the 1418 cm^{-1} band corresponds to bicarbonate species (HCO_3^-).[62,63] Their progressive growth with temperature indicates the occurrence of deep oxidation processes. By ~200 °C, the characteristic bands of CO_2 and H_2O become apparent and continue to intensify. As shown in Fig. 6d, the acetone band (~1700 cm^{-1}) increases at 150 °C and gradually decreases, turning into a negative band by 350 °C. The carboxylate (COO^-) band at 1610 cm^{-1} appears later, first intensifying and then disappearing at higher temperatures. The carbonate bands (1550 cm^{-1} and 1530 cm^{-1}) correlate with the decline of carboxylates. These observations support a multi-step oxidation pathway: propane is initially dehydrogenated to form intermediates such as propylene, acetone, and

View Article Online
DOI: 10.1039/D6EY00068A

propionaldehyde, which are further oxidized to carboxylates and carbonates, and eventually fully mineralized to CO_2 and H_2O.

For the SO_2-containing atmosphere study, the experimental procedure was identical to that under air, except that the reaction gas was replaced with air containing 30 ppm SO_2 after N_2 purging. Fig. 6e-g display the in-situ DRIFTS spectra of propane oxidation over $Ni_1Co_{0.5}AlO_x$@Pt/ZSM-5(3%) catalyst in air containing 30 ppm SO_2. At 40 °C, positive bands of propane (-CH_3 and -CH_2-) appear in the 2800-3100 cm^{-1} region. These bands rapidly invert to negative at 100 °C and become more pronounced with increasing temperature, indicating progressive propane consumption. Compared to the reaction in pure air in Fig. 6b, SO_2 presence leads to stronger initial adsorption bands, a sharper inversion, and greater negative intensity at the same temperatures, suggesting that SO_2 accelerates propane consumption, consistent with the previously observed slow increase in propane conversion upon SO_2 introduction. A band at 1271 cm^{-1} corresponds to physically adsorbed SO_2, while the 1408 cm^{-1} peak is attributed to SO_3, indicating that SO_2 not only adsorbs on the catalyst surface but also undergoes partial oxidation.[4] This competitive adsorption of SO_2 may temporarily block active sites, while the formation of SO_3 may further interact with Pt species. Additionally, bands at 860 and 1317 cm^{-1} are assigned to symmetric S-O-S vibrations and Pt-bound sulfite species, while peaks at 1346 and 1480 cm^{-1} correspond to the asymmetric S=O stretching of surface sulfate species.[23,39] These results confirm that SO_2 reacts with Pt active sites to form sulfite and sulfate species, which are likely responsible for irreversible catalyst deactivation. Nevertheless, the evolution of reaction

View Article Online
DOI: 10.1039/D6EY00068A

intermediates in the presence of SO_2 in Fig. 6g remains similar to that under SO_2-free conditions in Fig. 6d, suggesting that the overall oxidation pathway remains largely unaffected despite SO_2 interference.

Based on the analysis of the above characterizations, the possible mechanism for the $Ni_1Co_{0.5}AlO_x$@Pt/ZSM-5(3%) catalyst's optimal activity and H_2O/SO_2 resistance in propane oxidation was shown in Fig. 6h. The high activity originates from the synergistic presence of metallic Pt^0, Co^{3+}, O_{ads} and appropriately distributed weak and medium-strong acid sites. Together with the strong redox capacity of the composite, these features facilitate propane adsorption, C-H bond activation and subsequent complete oxidation. The excellent H_2O/SO_2 tolerance is attributed to the following two key factors. (1) The ZSM-5 shell physically hinders the diffusion of SO_2 and H_2O molecules over the active core. (2) The Si-O-Si framework of ZSM-5 exhibits intrinsic hydrophobicity, thereby weakening interactions with polar H_2O molecules. While these cations display lower reactivity toward H_2O and SO_2, the lattice oxygen enhances oxygen replenishment, effectively mitigating active-site poisoning. Collectively, these structural and interfacial features enable the $Ni_1Co_{0.5}AlO_x$@Pt/ZSM-5(3%) catalyst to achieve efficient propane oxidation with outstanding stability under humid and sulfur-containing conditions.

To further elucidate the water resistance mechanism of the catalysts, H_2O-TPD characterization was performed on $Pt/Ni_1Co_{0.5}AlO_x$ and $Ni_1Co_{0.5}AlO_x$@Pt/ZSM-5(3%) catalysts, with results strongly corroborating the aforementioned catalytic performance trends. The H_2O-TPD curves revealed that the total desorption peak area for

View Article Online
DOI: 10.1039/D6EY00068A

$Ni_1Co_{0.5}AlO_x$@Pt/ZSM-5(3%) was significantly smaller than that for Pt/$Ni_1Co_{0.5}AlO_x$, indicating that the core-shell structure with a ZSM-5 shell effectively reduced the total amount of adsorbed H_2O on the catalyst surface (Fig. 7a). This directly validates the prior conclusion: the ZSM-5 shell inhibits H_2O adsorption, thereby mitigating competitive adsorption between H_2O and reaction intermediates on propane/O_2/active sites (Fig. 7b). In contrast, $Ni_1Co_{0.5}AlO_x$@Pt/ZSM-5(3%) predominantly exhibited low-temperature desorption peaks, indicating weaker and reversible H_2O adsorption with minimal permanent damage to active sites. This aligns with its slight activity decay during water resistance testing and rapid recovery after dehydration. $Ni_1Co_{0.5}AlO_x$@Pt/ZSM-5(3%) exhibits fewer and more concentrated desorption peaks, attributed to the ZSM-5 shell's high Si/Al ratio reducing polar bond density while increasing non-polar Si-O-Si bonds, thereby weakening interactions between polar H_2O molecules and active sites. The hydrophobic Pt/ZSM-5 shell in $Ni_1Co_{0.5}AlO_x$@Pt/ZSM-5(3%) further impedes H_2O penetration and shields Pt and Co active sites from aqueous erosion, constituting the key to its exceptional H_2O stability. Collectively, H_2O-TPD results provide direct microscopic evidence for the water resistance mechanism of the core-shell catalyst, confirming that the ZSM-5 shell enhances water resistance by modulating the adsorption capacity, strength, and reversibility of H_2O.

To further elucidate the exceptional SO_2 tolerance of the core-shell catalysts, SO_2-TPD measurements were conducted on Pt/$Ni_1Co_{0.5}AlO_x$ and $Ni_1Co_{0.5}AlO_x$@Pt/ZSM-5(3%) to complement the previously discussed catalytic performance and structural

View Article Online
DOI: 10.1039/D6EY00068A

characterization (Fig. 7c and d). According to established taxonomies, low-temperature peaks (< 300 °C) correspond to weakly adsorbed SO_2 at volatile sites, the mid-temperature peak (300-600 °C) indicates moderately adsorbed SO_2 at acidic or redox-active sites, while the high-temperature peak (> 600 °C) reflects strongly bound SO_2 at irreversible sulfidated sites. As depicted in Fig. 7c, $Pt/Ni_1Co_{0.5}AlO_x$ exhibits pronounced desorption peaks across the entire temperature range, with low-temperature desorption peaks predominating. This phenomenon confirms that unprotected Pt and Co sites exhibit strong adsorption of SO_2, consistent with their severe deactivation in SO_2 environments. In stark contrast, $Ni_1Co_{0.5}AlO_x$@Pt/ZSM-5(3%) exhibits negligible desorption at elevated temperatures, with low-to-medium temperature peaks accounting for over 90% of the total desorption area. These peaks correspond to SO_2 adsorption on weak-to-moderate Lewis acid sites within the ZSM-5 shell, where SO_2 is captured through weak interactions. In-situ DRIFTS experiments further corroborate this mechanism: sulfate/sulfite species were detected on the ZSM-5 surface, with no Pt sulfidation observed. Notably, $Ni_1Co_{0.5}AlO_x$@Pt/ZSM-5(3%) exhibits a faint desorption peak around 410 °C, indicating minor sulfate/sulfite formation. This phenomenon aligns closely with the catalyst's enhanced catalytic activity during SO_2 exposure, further validating its ability to mitigate sulfur poisoning through controlled SO_2 adsorption. This core-shell interface-driven adsorption mechanism explains why $Ni_1Co_{0.5}AlO_x$@Pt/ZSM-5(3%) preferentially adsorbs SO_2 within the shell layer, thereby shielding Pt^0 and Co^{3+} from sulfidation and maintaining catalytic activity even under SO_2 exposure. In summary, the ZSM-5 shell forms a selective barrier via

View Article Online
DOI: 10.1039/D6EY00068A

interfacially engineered acidic sites, confining SO_2 within the shell and preventing its diffusion to Pt and Co active sites. This confers exceptional sulfur resistance unattainable by bare $Pt/Ni_1Co_{0.5}AlO_x$.

To elucidate the atomic-level details of propane activation mechanisms, DFT calculations were employed to compare the adsorption energies of propane on $Pt/NiCoAlO_x$ and $NiCoAlO_x$@Pt/ZSM-5 model surfaces. As shown in Fig. 8a, the adsorption energy of propane on $NiCoAlO_x$@Pt/ZSM-5 surface is -0.52 eV, which is more negative than that on $Pt/NiCoAlO_x$ surface (-0.50 eV). A more negative adsorption energy indicates stronger interactions between propane and the catalyst surface, which favors the cleavage of the inert C-H bond. Fig. 8b and c present differential charge density plots for $Pt/NiCoAlO_x$ and $NiCoAlO_x$@Pt/ZSM-5 models. These reveal strong pairwise interactions among the Pt, $NiCoAlO_x$, and ZSM-5 phases, with electron transfer between Pt and oxygen atoms on both $NiCoAlO_x$ and ZSM-5. Fig. 8d elucidates the molecular-level reaction pathway for propane oxidation catalyzed on $NiCoAlO_x$@Pt/ZSM-5. Propane first adsorbs onto the catalyst surface. Pt^0 sites on the Pt/ZSM-5 shell cleave the inert C-H bond, yielding propene as the first intermediate. The propylene is further oxidized to form acetone-like species (C_3H_6O), followed by a carboxylate intermediate ($C_3H_6O_2$). The formation of these oxygen-containing species was confirmed by in-situ DRIFTS. The carboxylate intermediates were broken into smaller oxygen-containing species (CH_3O-, C_2H_3O-), which are subsequently fully oxidized to CO_2 and H_2O. The reaction pathway for the oxidative decomposition of propane on the $Pt/NiCoAlO_x$ model is shown in Fig. S18. Additionally, we analyzed

View Article Online
DOI: 10.1039/D6EY00068A

the Gibbs free energy changes for the oxidation of propane over Pt/$NiCoAlO_x$ and $NiCoAlO_x$@Pt/ZSM-5. As depicted in Fig. 8e, the reaction traverses five intermediate states (IS1-IS5) and four transition states (TS1-TS4), with Gibbs free energy barriers (ΔG) quantified for each step.[64-66] The Gibbs free energy barrier (ΔG_1) for $NiCoAlO_x$@Pt/ZSM-5 is 1.35 eV, markedly lower than that for Pt/$NiCoAlO_x$ (1.58 eV). This reduction indicates that the $NiCoAlO_x$@Pt/ZSM-5 structure promotes the activation of propane's initial C-H bond, consistent with our experimental observations. Compared to Pt/$NiCoAlO_x$'s ΔG_2 of 1.25 eV, $NiCoAlO_x$@Pt/ZSM-5 exhibits a ΔG_2 of 1.06 eV. This further reduction in the energy barrier indicates that the ZSM-5 shell stabilizes the reaction intermediate through strong interactions at acid sites, thereby lowering the energy required for subsequent oxidation.[64] The ΔG_3 value for $NiCoAlO_x$@Pt/ZSM-5 (0.82 eV) is lower than that for Pt/$NiCoAlO_x$ (0.98 eV), attributed to synergistic electronic modulation at the Pt/ZSM-5 interface. The ZSM-5 shell redistributes electrons on Pt, enhancing the reactivity of the adsorbed intermediate towards lattice oxygen from the $CoNiAlO_x$ core. In the final deep oxidation step, the energy barrier for $NiCoAlO_x$@Pt/ZSM-5 (ΔG_4 = 1.01 eV) is lower than that for Pt/$NiCoAlO_x$ (1.16 eV), thereby ensuring efficient conversion of the intermediate into CO_2 and H_2O.[65] The geometric structural parameters of propane adsorbed on Pt/$NiCoAlO_x$ and $NiCoAlO_x$@Pt/ZSM-5 surfaces are shown in Table S2. The $NiCoAlO_x$@Pt/ZSM-5 surface exhibit greater elongation of C-C bonds and greater distortion of bond angles than on Pt/$NiCoAlO_x$, indicating that $NiCoAlO_x$@Pt/ZSM-5 exerts a more pronounced structural distortion -hydrogen bonds, indicating that

View Article Online
DOI: 10.1039/D6EY00068A

$NiCoAlO_x$@Pt/ZSM-5 exerts more pronounced structural distortion and bond activation effects on propane. This aligns with the preceding analysis of DFT adsorption energies and reaction energy barriers, providing a geometric explanation for $NiCoAlO_x$@Pt/ZSM-5's superior propane oxidation activity.

To gain deeper insight into the water resistance mechanism of the catalyst, we compared the adsorption energies of H_2O on Pt/$NiCoAlO_x$ and $NiCoAlO_x$@Pt/ZSM-5, with results shown in Fig. 8f. The adsorption energy of H_2O on Pt/$NiCoAlO_x$ (-0.81 eV) is markedly more negative than that on $NiCoAlO_x$@Pt/ZSM-5 (-0.52 eV), directly accounting for the superior water resistance of $NiCoAlO_x$@Pt/ZSM-5. In contrast, Pt/$NiCoAlO_x$ contains more polar metal hydroxyl sites, leading to intense competition between H_2O and propane for Pt active sites. Further analysis of surface energy changes via density of states (DOS) modelling is presented in Fig. 8g and h. Pt/$NiCoAlO_x$ and $NiCoAlO_x$@Pt/ZSM-5 exhibit distinct density of states distributions owing to the structural differences between the spinel $NiCoAlO_x$ and ZSM-5 frameworks. Nevertheless, both systems display rich band structures near the Fermi level, indicating that both the spinel structure of $NiCoAlO_x$ and the ZSM-5 framework facilitate electron transfer at the surface.[66] To elucidate the activation mechanism of oxygen species on Pt/$NiCoAlO_x$ and $NiCoAlO_x$@Pt/ZSM-5, we analyzed the adsorption and dissociation of O_2 on both models (Fig. 8i). The O_2 adsorption energy on $NiCoAlO_x$@Pt/ZSM-5 is -0.32 eV, lower than that on Pt/$NiCoAlO_x$ (-0.60 eV). This indicates that the adsorption strength of oxygen species on $NiCoAlO_x$@Pt/ZSM-5 is favorable, preventing dissociation from being hindered by an excessively stable O-O bond. In contrast, O_2

View Article Online
DOI: 10.1039/D6EY00068A

exhibits stronger adsorption on Pt/NiCoAlO$_x$, potentially leading to slower O-O bond cleavage. Fig. 8j analyzes the Projected Density of States (PDOS) for Pt, the primary active component in the model structures. It is evident that under the combined influence of NiCoAlO$_x$ and ZSM, the d-band center of Pt in NiCoAlO$_x$@Pt/ZSM-5 (-1.004 eV) shifts towards the Fermi level compared to Pt/NiCoAlO$_x$ (-1.324 eV). This indicates that the synergistic interaction between NiCoAlO$_x$ and ZSM elevates the energy of surface Pt. Bader charges corroborate the PDOS findings (Table S3). The triphasic electron transfer between the Pt/ZSM structure and NiCoAlO$_x$ is discernible, ultimately leading to macroscopic electron transfer from Co and Al in NiCoAlO$_x$ to Pt and Ni. This significantly enhances catalytic performance.[64,66]

To elucidate the molecular mechanisms underlying the SO_2 resistance of Pt/NiCoAlO$_x$ and NiCoAlO$_x$@Pt/ZSM-5, we analyzed the Gibbs free energy curves for SO_2 adsorption and oxidation on the surfaces of Pt/NiCoAlO$_x$ and NiCoAlO$_x$@Pt/ZSM-5 (Fig. 8k). The SO_2 adsorption energy on NiCoAlO$_x$@Pt/ZSM-5 is -0.44 eV, lower than the -0.52 eV observed on Pt/NiCoAlO$_x$. SO_2 is captured by the ZSM-5 shell, avoiding the formation of irreversible bonds, in stark contrast to the excessively strong SO_2 adsorption on Pt/NiCoAlO$_x$. The free energy barrier for SO_2 oxidation (ΔG from SO_2 (g) to SO_2-O*) in the iCoAlO$_x$@Pt/ZSM-5 system is 0.70 eV, markedly higher than that of Pt/NiCoAlO$_x$ (0.13 eV). This elevated barrier inhibits the formation of SO_3* (an irreversible Pt sulfide precursor) on the NiCoAlO$_x$@Pt/ZSM-5 surface. Conversely, the low energy barrier in Pt/NiCoAlO$_x$ promotes SO_2 oxidation to SO_3*, which readily reacts with Pt to form deactivated Pt-S species. The adsorption

View Article Online
DOI: 10.1039/D6EY00068A

energy for SO_3* on $NiCoAlO_x$@Pt/ZSM-5 is -0.24 eV, substantially lower than the -0.48 eV observed on Pt/$NiCoAlO_x$. The weak adsorption of SO_3* on $NiCoAlO_x$@Pt/ZSM-5 ensures that any formed SO_3 is readily desorbed or captured by the ZSM-5 shell, thereby preventing its accumulation at Pt active sites.

5. Analysis and discussion about the relationship between textural properties and catalytic performance of catalyst

We systematically analyzed the intrinsic mechanisms underlying the exceptional catalytic activity, resistance to H_2O poisoning, and resistance to SO_2 poisoning exhibited by the $Ni_1Co_{0.5}AlO_x$@Pt/ZSM-5(3%) and $Ni_1Co_{0.5}AlO_x$@Pt/ZSM-5(5%) core-shell catalysts. The $Ni_1Co_{0.5}AlO_x$@Pt/ZSM-5(3%) catalyst demonstrated optimal activity. The $Ni_1Co_{0.5}AlO_x$@Pt/ZSM-5(3%) catalyst possesses the highest contents of Pt^0, Co^{3+}, and O_{ads}, all of which play irreplaceable roles in the propane oxidation reaction. The higher O_{ads} content in the $Ni_1Co_{0.5}AlO_x$@Pt/ZSM-5(3%) catalyst enables faster conversion of the propane intermediate, with highly mobile and active O_{ads} directly participating in the deep oxidation of the carboxylate intermediate to CO_2 and H_2O. The 3 wt% Pt/ZSM-5 shell thickness directly influences diffusion resistance for propane and O_2 towards active sites, constituting a key factor distinguishing the activity of $Ni_1Co_{0.5}AlO_x$@Pt/ZSM-5(3%) from other catalysts. Conversely, medium-strong acid sites originating from ZSM-5-bridged Si-OH-Al groups and unsaturated Co^{3+}/Ni^{3+} coordination in the core region promote C-H bond cleavage by donating protons to propane. The lower E_a value of $Ni_1Co_{0.5}AlO_x$@Pt/ZSM-5(3%) confirms that abundant weak and medium-strong acid sites reduce the energy barrier for C-H bond activation.

View Article Online
DOI: 10.1039/D6EY00068A

The mechanisms underlying the resistance to H_2O poisoning in $Ni_1Co_{0.5}AlO_x$@Pt/ZSM-5(3%) and $Ni_1Co_{0.5}AlO_x$@Pt/ZSM-5(5%) were further explored in depth. The hydrophobicity of the Pt/ZSM-5 shell constitutes the primary defence mechanism against H_2O adsorption. This shell forms a physical barrier that prevents H_2O diffusion into the $Ni_1Co_{0.5}AlO_x$ core, thereby safeguarding the redox active species from degradation. The non-polar Si-O-Si bonds exhibit weak interactions with polar H_2O molecules. In contrast, the exposed Pt/$Ni_1Co_{0.5}AlO_x$ surface is rich in polar Al-OH hydroxyl groups, rendering it highly susceptible to H_2O adsorption. The lower surface O_{wat} for $Ni_1Co_{0.5}AlO_x$@Pt/ZSM-5(3%) and $Ni_1Co_{0.5}AlO_x$@Pt/ZSM-5(5%) catalysts compared to bare Pt/$Ni_1Co_{0.5}AlO_x$, reducing available H_2O adsorption sites. The Pt^0 content on the surfaces of $Ni_1Co_{0.5}AlO_x$@Pt/ZSM-5(3%) and Pt^0 species readily deactivate under aqueous conditions, progressively oxidizing to Pt^{2+} or Pt^{4+}, whereas the ZSM-5 shell significantly mitigates this oxidation reaction. This explains why the T_{90} of $Ni_1Co_{0.5}AlO_x$@Pt/ZSM-5(3%) remains lower than that of the bare Pt/$Ni_1Co_{0.5}AlO_x$ catalyst under aqueous conditions.

We investigated the sulfur tolerance of the $Ni_1Co_{0.5}AlO_x$@Pt/ZSM-5 catalyst. The $Ni_1Co_{0.5}AlO_x$@Pt/ZSM-5(3%) catalyst demonstrated exceptional SO_2 tolerance, exhibiting enhanced activity during SO_2 exposure, whereas the bare catalyst's activity declined to 44.2%. This tolerance stems from the SO_2 trapping and active site protection mechanisms within the shell layer. Acid sites within the ZSM-5 shell preferentially adsorb SO_2, thereby reducing its contact with Pt active sites. Even in the presence of SO_2, the $Ni_1Co_{0.5}AlO_x$@Pt/ZSM-5(3%) catalyst maintained the normal propane

View Article Online
DOI: 10.1039/D6EY00068A

oxidation pathway, avoiding activity loss due to pathway disruption. The minor sulfate species formed on the Pt/ZSM-5 shell surface act as strong Lewis acids, further promoting propane adsorption and C-H bond activation. This explains the transient increase in activity observed for $Ni_1Co_{0.5}AlO_x$@Pt/ZSM-5(3%) during SO_2 exposure.

Based on the above discussion and analysis, a correlation between the structure and performance of the $Ni_1Co_{0.5}AlO_x$@Pt/ZSM-5(x%) (x=3, 5) catalysts can be summarized, arising from synergistic effects between the core and shell. The $Ni_1Co_{0.5}AlO_x$ core provides abundant Co^{3+} and Ni^{3+} species and active oxygen species, whilst the Pt/ZSM-5 shell supplies Pt^0 active sites, a hydrophobic protective layer, and SO_2 capture sites. The core-shell interface facilitates electron transfer and oxygen species exchange, thereby enhancing overall catalytic performance. The 3 wt% and 5 wt% Pt/ZSM-5 shells strike a balance between activity and stability, rendering $Ni_1Co_{0.5}AlO_x$@Pt/ZSM-5(3%) suitable for low-temperature, high-activity, harsh industrial environments. More satisfactorily, compared to previously reported platinum-based catalysts for propane oxidation, $Ni_1Co_{0.5}AlO_x$@Pt/ZSM-5(3%) and $Ni_1Co_{0.5}AlO_x$@Pt/ZSM-5(5%) catalysts demonstrate significant advantages in both activity and resistance to poisoning. This confirms that the supramolecular assembly strategy for core-shell catalysts represents an effective approach to overcoming industrial application bottlenecks for Pt-based VOCs oxidation catalysts.

Although the $Ni_1Co_{0.5}AlO_x$@Pt/ZSM-5(3%) catalyst exhibits excellent activity and resistance to water and sulphur in propane oxidation, it still has certain limitations that warrant further investigation. The catalyst's optimal performance is observed under

View Article Online
DOI: 10.1039/D6EY00068A

low to moderate concentrations of H_2O and SO_2. Its stability at higher concentrations of poisons or during long-term industrial operation remains to be verified. For instance, the preparation process involves hydrothermal coating and precise control of the shell thickness; the process costs and reproducibility for scaled-up production require optimization. In this study, propane was used as a model alkane reactant; the catalyst's applicability to other VOCs, such as toluene and chlorinated hydrocarbons, has not yet been investigated. We will conduct systematic research on the above issues in the future to further advance the practical industrial application of this core-shell catalytic system.

6. Conclusion

In summary, we rationally designed and prepared a series of $Ni_1Co_{0.5}AlO_x$@Pt/ZSM-5 core-shell catalysts by supramolecular assembly coupled with hydrothermal coating to address the key issue of poor H_2O/SO_2 resistance in Pt-based catalysts for propane catalytic oxidation. The catalytic activity and anti-poisoning performance were improved. The Si-O-Si linkages in the ZSM-5 shell exhibited low affinity for polar H_2O molecules, significantly enhancing hydrophobicity and thereby suppressing H_2O adsorption. Simultaneously, acidic sites within the ZSM-5 shell preferentially adsorb SO_2, thereby reducing its contact with Pt active sites. This enables the $Ni_1Co_{0.5}AlO_x$@Pt/ZSM-5 catalyst to exhibit outstanding sulfur tolerance. The shell acts not only as a physical barrier preventing H_2O and SO_2 from reaching active sites, but also as a chemical interface that promotes the formation and stabilization of high-valence metal ions such as Pt^{4+}, Co^{3+}, Ni^{3+} and lattice oxygen. $Ni_1Co_{0.5}AlO_x$@Pt/ZSM-5(3%) catalyst exhibits optimal catalytic activity and SO_2 tolerance, along with

View Article Online
DOI: 10.1039/D6EY00068A

improved H_2O resistance. The reason is attributed to the highest contents of Pt^0, Co^{3+} and adsorbed oxygen, which enhanced redox capability and acid sites, synergistically facilitating the adsorption and deep oxidation of propane. These findings provide a promising strategy for designing Pt-based catalysts with enhanced activity and stability in H_2O- and SO_2-containing environments.

Declaration of competing interest

The authors confirm that neither personal affiliations nor financial stakes had any impact on the content of this article.

Date availability

The data that support the findings of this study are available in the supporting information of this article. Supporting information including the results from TEM, HRTEM, catalytic activity, reaction kinetics calculations, XRD, BET, H_2-TPR, O_2-TPD, NH_3-TPD, in-situ DRIFTS and DFT calculations.

Acknowledgement

This work was supported by the Science and Technology Program of Chengguan District (2024-rc-4), Key Research and Development Program of Gansu Province (24YFFA011), West Light Foundation of Chinese Academy of Sciences (xbzg-zdsys-202318), Shandong Provincial Natural Science Foundation (No. ZR2025QC98).

View Article Online
DOI: 10.1039/D6EY00068A

References

1. C. He, J. Cheng, X. Zhang, M. Douthwaite, S. Pattisson, Z. Hao, Recent Advances in the Catalytic Oxidation of Volatile Organic Compounds: A Review Based on Pollutant Sorts and Sources, Chem. Rev., 2019, **119**, 4471-4568.

2. R. Tang, Z. Peng, F. Liu, Z. Zhang, X. Yang, Y. Zhang, Facet-engineered Au/CeO_2 catalysts enabling light-assisted non-oxidativemethane coupling via spatially separated reaction functions, Chem. Eng. J., 2026, **538**, 176765.

3. F. Dong, W. Han, W. Han, Z. Tang, Assembling core-shell SiO_2@$Ni_aCo_bO_x$ nanotube decorated by hierarchical NiCo-Phyllisilicate ultrathin nanosheets for highly efficient catalytic combustion of VOCs, Appl. Catal. B: Environ. Energy, 2022, **315**, 121524.

4. S. Wu, C. Feng, F. Dong, S. Ma, W. Han, W. Han, H. Zhang, Z. Tang, Tailored $CoNiO_x$@$CuVO_x$ core-shell catalyst exhibiting strong charge transfer and SO_2 tolerance for efficient elimination of propane, Appl. Catal. B: Environ. Energy, 2025, **372**, 125293.

5. J. Liu, R. Burciaga, S. Tang, S. Ding, H. Ran, W. Zhao, G. Wang, Z. Zhuang, L. Xie, Z. Lyu, Y. Lin, A. Du, A. Yuan, J. Fu, B. Song, J. Zhu, Z. Sun, X. Jin, Z.-Y. Huo, B. Shen, M. Shen, Y. Cao, Y. Zhou, Y. Jiang, D. Zhu, M. Sun, X. Wu, C. Qin, Z. Jiang, O. Metin, C.J. Thambiliyagodage, J.-J. Lv, Q. Li, H. Wu, Z. Wu, J.C.-H. Lam, G. Gao, C. Li, M. Luo, Y. Jiang, X. Wang, J. Li, M. Liu, R. Lin, H. Ren, B. Han, Y. Jing, W. Zhu, Heterogeneous catalysis for the environment, The Innovation Materials, 2024, **2**, 100090.

View Article Online
DOI: 10.1039/D6EY00068A

6. Q. Peng, W. Han, W. Han, F. Dong, Z. Tang, Z. Zhou, Tailored Pt/$Ni_aCo_bAlO_x$ catalysts derived from LDH structure for efficient catalytic combustion of propane, Chem. Eng. J., 2024, **500**, 157181.

7. Z. Huang, J. Ding, X. Yang, H. Liu, P. Song, Y. Guo, Y. Guo, L. Wang, W. Zhan, Highly Efficient Oxidation of Propane at Low Temperature over a Pt-Based Catalyst by Optimization Support, Environ. Sci. Technol., 2022, **56**, 17278-17287.

8. S. Tao, X. Wang, C. Rao, K. Liu, Y. Li, Z. Yuan, G. Peng, Y. Lou, J. Ye, H. Liu, Z. Zhang, X. Yang, Y. Zhang, S. Song, A Smart Catalytic System with In Situ Dynamic Current-Tuned Pd-Ce Diatomic Interactions for Enhanced Methane Oxidation, Adv. Funct. Mater., 2026, **36**, e19202.

9. Y.-Y. Li, Y. Ren, J. He, H. Xiao, J.-R. Li, Recent Advances of the Effect of H_2O on VOC Oxidation over Catalysts: Influencing Factors, Inhibition/Promotion Mechanisms, and Water Resistance Strategies, Environ. Sci. Technol., 2025, **59**, 1034-1059.

10. G. Fan, F. Li, D.G. Evans, X. Duan, Catalytic applications of layered double hydroxides: recent advances and perspectives, Chem. Soc. Rev., 2014, **43**, 7040-7066.

11. J. Xu, B. Xie, Z. Zhang, Z. Lu, X. Yan, N. Meng, X. Zhou, K. Liu, C. Rao, G. Hu, X. Yang, Y. Zhang, Hydride Vacancy-Driven Photothermal C-H Activation over Ni/TiH_2 Catalysts, ACS Catal., 2026, **16**, 8669-8681.

12. S. He, Z. An, M. Wei, D.G. Evans, X. Duan, Layered double hydroxide-based catalysts: nanostructure design and catalytic performance, Chem. Commun., 2013, **49**, 5912-5920.

View Article Online
DOI: 10.1039/D6EY00068A

13. J. Feng, Y. He, Y. Liu, Y. Du, D. Li, Supported catalysts based on layered double hydroxides for catalytic oxidation and hydrogenation: general functionality and promising application prospects, Chem. Soc. Rev., 2015, **44**, 5291-5319.

14. G. Meng, J. Sun, L. Tao, K. Ji, P. Wang, Y. Wang, X. Sun, T. Cui, S. Du, J. Chen, D. Wang, Y. Li, Ru_1Co_n Single-Atom Alloy for Enhancing Fischer-Tropsch Synthesis, ACS Catal., 2021, **11**, 1886-1896.

15. Z. Zhang, J. Wang, X. Ge, S. Wang, A. Li, R. Li, J. Shen, X. Liang, T. Gan, X. Han, X. Zheng, X. Duan, D. Wang, J. Jiang, Y. Li, Mixed Plastics Wastes Upcycling with High-Stability Single-Atom Ru Catalyst, J. Am. Chem. Soc., 2023, **145**, 22836-22844.

16. R. Li, T. Xue, R. Bingre, Y. Gao, B. Louis, Q. Wang, Microporous Zeolite@Vertically Aligned Mg-Al Layered Double Hydroxide Core@Shell Structures with Improved Hydrophobicity and Toluene Adsorption Capacity under Wet Conditions, ACS Appl. Mater. Interfaces, 2018, **10**, 34834-34839.

17. Z. Fu, G. Zhang, W. Han, Z. Tang, The water resistance enhanced strategy of Mn based SCR catalyst by construction of TiO_2 shell and superhydrophobic coating, Chem. Eng. J., 2021, **426**, 131334.

18. B. Bensafi, N. Chouat, F. Djafri, The universal zeolite ZSM-5: Structure and synthesis strategies. A review, Coordin. Chem. Rev., 2023, **496**, 215397.

19. C. Wang, H. Guo, S. Leng, J. Yu, K. Feng, L. Cao, J. Huang, Regulation of hydrophilicity/hydrophobicity of aluminosilicate zeolites: a review, Crit. Rev. Solid State, 2021, **46**, 330-348.

20. L. Wang, F. Dong, W. Han, Z. Tang, Engineering a Mesoporous Pt/Ce-ZSM-5

Catalyst by a Confined Encapsulation Strategy for Low-Temperature Catalytic Combustion of Toluene, Ind. Eng. Chem. Res., 2024, **63**, 22354-22368.

21. R.S. Ghosh, T.T. Le, T. Terlier, J.D. Rimer, M.P. Harold, D. Wang, Enhanced Selective Oxidation of Ammonia in a Pt/Al_2O_3@Cu/ZSM-5 Core-Shell Catalyst, ACS Catal., 2020, **10**, 3604-3617.

22. S. Wu, F. Dong, H. Zhang, Z. Tang, Targeted design strategies of sulfur-tolerant catalysts for catalytic combustion of VOCs: From atomic-scale mechanisms to application prospects, Coordin. Chem. Rev., 2026, **557**, 217699.

23. G. Corro, R. Montiel, C. Vázquez L, Promoting and inhibiting effect of SO_2 on propane oxidation over Pt/Al_2O_3, Catal. Commun., 2002, **3**, 533-539.

24. M.Y. Smirnov, A.V. Kalinkin, A.V. Pashis, I.P. Prosvirin, V.I. Bukhtiyarov, Interaction of SO_2 with Pt Model Supported Catalysts Studied by XPS, Phys. Chem. C, 2014, **118**, 22120-22135.

25. P. Yang, J. Li, L. Bao, X. Zhou, X. Zhang, S. Fan, Z. Chen, S. Zuo, C. Qi, Adsorption/catalytic combustion of toxic 1, 2-dichloroethane on multifunctional Nb_2O_5-TiO_2 composite metal oxides, Chem. Eng. J., 2019, **361**, 1400-1410.

26. S. Sharma, A. Paul, Evolution of Ultrathin CoFe-Nanomesh for Oxygen Evolution Reaction: From Slit Pores to Ink-Bottle Pores, Chem.-Asian J., 2025, **20**, e202401156.

27. Z. Yan, Z. Xu, L. Yue, L. Shi, L. Huang, Hierarchical Ni-Al hydrotalcite supported Pt catalyst for efficient catalytic oxidation of formaldehyde at room temperature, Chinese J. Catal., 2018, **39**, 1919-1928.

28. W. Zhao, Y. Xu, Y. Qiao, R. Sun, J. Qian, Y. Wang, Q. Liu, Z. Shi, F. Meng, X.

Zhan, Q. Zhang, The design of core-shell ZSM-5@NiAl-LDH composites for efficient adsorption of VOCs under high humidity, Sep. Purif. Technol., 2025, **355**, 129729.

29. M. Amanati, M. Kazemeini, S. Soltanali, S.J. Royaee, Tailor making of a green zeolite-based catalyst for propane dehydrogenation: Impact of metal incorporation upon the stability and selectivity of Co/HZSM-5, Chem. Eng. J., 2025, **519**, 165360.

30. W. Ben Soltan, J. Sun, W. Wang, J. Peng, Y. Zhang, T. Wang, Y. Chang, L. Ding, Z. Cao, W. Wang, H. Liu, Modification of Fe on hydrophobic ZSM-5 zeolite: Optimization of adsorption and catalytic performance for decomposition of VOCs at low-temperature, Sep. Purif. Technol., 2024, **333**, 125908.

31. I.G. Wenzel, O.W. Perez-Lopez, Hydrogen production by ethanol steam reforming over Ni-Co-Al mixed oxides derived from LDH, J. Porous Mat., 2024, **31**, 69-80.

32. W. Deng, Q. Tang, S. Huang, L. Zhang, Z. Jia, L. Guo, Low temperature catalytic combustion of chlorobenzene over cobalt based mixed oxides derived from layered double hydroxides, Appl. Catal. B: Environ. Energy, 2020, **278**, 119336.

33. K.S. Triantafyllidis, L. Nalbandian, P.N. Trikalitis, A.K. Ladavos, T. Mavromoustakos, C.P. Nicolaides, Structural, compositional and acidic characteristics of nanosized amorphous or partially crystalline ZSM-5 zeolite-based materials, Micropor. Mesopor. Mat., 2004, **75**, 89-100.

34. Y. Tian, L. Guo, C. Qiao, Z. Sun, Y. Yamauchi, S. Liu, Dynamics-driven tailoring of sub-nanometric Pt-Ni bimetals confined in hierarchical zeolite for catalytic hydrodeoxygenation, Appl. Catal. B: Environ. Energy, 2023, **336**, 122945.

35. C. Wan, X. Wei, G. Cai, D. Li, Y. Zhan, Y. Xiao, L. Jiang, Hydrotalcite-derived

View Article Online
DOI: 10.1039/D6EY00068A

aluminum-doped cobalt oxides for catalytic benzene combustion: Effect of calcination atmosphere, Mol. Catal., 2022, **520**, 112160.

36. X. Cai, X. Shen, L. Ma, Z. Ji, C. Xu, A. Yuan, Solvothermal synthesis of NiCo-layered double hydroxide nanosheets decorated on RGO sheets for high performance supercapacitor, Chem. Eng. J., 2015, **268**, 251-259.

37. R. Duddi, Shivani, S. Dhiman, N. Kamboj, S. Kumar, Facile single-step synthesis of a hierarchical structure of NiCo-LDH on carbon cloth as cathode material in high-performance Zn-ion capacitors, Solid State Sci., 2023, **143**, 107289.

38. W. Li, J. Tu, J. Sun, Y. Zhang, J. Fang, M. Wang, X. Liu, Z.-Q. Tian, F. Ru Fan, Boosting Reactive Oxygen Species Generation via Contact-Electro-Catalysis with FeIII-Initiated Self-cycled Fenton System, Angew. Chem. Int. Ed., 2025, **64**, e202413246.

39. D. Yang, F. Dong, J. Wang, Z. Tang, J. Zhang, Constructing a core-shell Pt@MnO_x/SiO_2 catalyst for benzene catalytic combustion with excellent SO_2 resistance: new insights into active sites, Environ. Sci. Nano, 2024, **11**, 1926-1947.

40. S. Zhang, Y. Li, C. Ding, Y. Niu, Y. Zhang, B. Yang, G. Li, J. Wang, Z. Ma, L.-J. Yu, Atomic Dispersion of Pt Clusters Encapsulated Within ZSM-5 Depending on Aluminum Sites and Calcination Temperature, Small Struct., 2023, **4**, 2200115.

41. H. Ohtsuka, The Oxidation of Methane at Low Temperatures Over Zirconia-Supported Pd, Ir and Pt Catalysts and Deactivation by Sulfur Poisoning, Catal. Lett., 2011, **141**, 413-419.

42. W. Zhu, Y. Li, C. Zhao, J. Luo, Y. Sun, C. Liang, Insights into the catalytic

performance of LDHs-derived CoAlO oxides with different anions intercalation for propane total oxidation, Appl. Surf. Sci., 2024, **642**, 158546.

43. F. Wu, F. Tian, M. Li, S. Geng, L. Qiu, L. He, L. Li, Z. Chen, Y. Yu, W. Yang, Y. Hou, Engineering Lattice Oxygen Regeneration of NiFe Layered Double Hydroxide Enhances Oxygen Evolution Catalysis Durability, Angew. Chem. Int. Ed., 2025, **64**, e202413250.

44. S. Liang, Y. Liao, Y. Lin, T. Zhang, H. Yang, X. Ma, Decarbonized core-shell-like structure: Enhancing Fe-based oxygen carriers for superior hydrogen selectivity and stability, Energy, 2024, **304**, 132072.

45. A.A. Ahmed, Z.H. Yamani, Synthesis and characterization of SnO_2-modified ZSM-5 zeolite for hydrogen gas sensing, Mater. Chem. Phys., 2021, **259**, 124181.

46. N. Siddiqui, C. Pendem, R. Goyal, R. Khatun, T.S. Khan, C. Samanta, K. Chiang, K. Shah, M. Ali Haider, R. Bal, Study of γ-valerolactone production from hydrogenation of levulinic acid over nanostructured Pt-hydrotalcite catalysts at low temperature, Fuel, 2022, **323**, 124272.

47. H. Shi, P. Yang, L. Huang, Y. Wu, D. Yu, H. Wu, Y. Zhang, P. Xiao, Single-atom Pt-CeO_2/Co_3O_4 catalyst with ultra-low Pt loading and high performance for toluene removal, J. Colloid Interf. Sci., 2023, **641**, 972-980.

48. Y. Yao, F. Yu, J. Li, J. Li, Y. Li, Z. Wang, M. Zhu, Y. Shi, B. Dai, X. Guo, Two-dimensional NiAl layered double oxides as non-noble metal catalysts for enhanced CO methanation performance at low temperature, Fuel, 2019, **255**, 115770.

49. M. Gil-Calvo, C. Jiménez-González, B. de Rivas, J.I. Gutiérrez-Ortiz, R. López-

View Article Online
DOI: 10.1039/D6EY00068A

Fonseca, Effect of Ni/Al molar ratio on the performance of substoichiometric $NiAl_2O_4$ spinel-based catalysts for partial oxidation of methane, Appl. Catal. B: Environ. Energy, 2017, **209**, 128-138.

50. S. Weber, K.L. Abel, R.T. Zimmermann, X. Huang, J. Bremer, L.K. Rihko-Struckmann, D. Batey, S. Cipiccia, J. Titus, D. Poppitz, C. Kübel, K. Sundmacher, R. Gläser, T.L. Sheppard, Porosity and Structure of Hierarchically Porous Ni/Al_2O_3 Catalysts for CO_2 Methanation, Catalysts, 2020, **10**, 1471.

51. Y. Jiang, F. Guo, L. Qiu, T. Liu, Y. Hu, W. Yang, Y. Liu, Y. Sun, Z. Wu, Y. Song, X. Guo, Enhancing the Integral Structural and Thermal Stability of Ultrahigh-Ni Cathodes via Morphology Refinement and In Situ Interfacial Engineering, ACS Appl. Mater. Interfaces., 2023, **15**, 35072-35081.

52. X. Feng, H. Chen, Q. Xue, C. Su, Y. Zhou, Construction of core-shell structured $CrO_x/NiCo_xO_4$ catalyst for low temperature catalytic oxidation of toluene: Understanding the reactivity promotion mechanism of the core-shell interactions, Chem. Eng. J., 2024, **490**, 151464.

53. A. Jha, Y.-L. Lee, W.-J. Jang, J.-O. Shim, K.-W. Jeon, H.-S. Na, H.-M. Kim, H.-S. Roh, D.-W. Jeong, S.G. Jeon, J.-G. Na, W.L. Yoon, Effect of the redox properties of support oxide over cobalt-based catalysts in high temperature water-gas shift reaction, Mol. Catal., 2017, **433**, 145-152.

54. X.-H. Guo, S.-Y. Sun, M.-X.-Z. Gao, Q.-G. Dai, W.-C. Zhan, L. Wang, Y. Guo, A.-Y. Wang, Y.-L. Guo, Highly efficient Ag/Ce-Zr catalyst for catalytic oxidation of NVOCs: balance of redox ability and acidity, Rare Metals, 2024, **43**, 6473-6485.

View Article Online
DOI: 10.1039/D6EY00068A

55. Y. Chen, H. Zhang, H. Li, J. Hu, Y. Long, M. Liu, Alumina catalyst with high density of medium acid sites for N-arylpyrrolidines synthesis, Appl. Catal.s A: General, 2022, **640**, 118668.

56. X. Bie, K. Jiao, C. Gong, B. Qu, D. Liu, S. Ma, The Role of Medium Acid Sites Tuned by Ce Adding in Moderate-Temperature NH_3-SCR, Catal. Lett., 2022, **152**, 2270-2279.

57. Z. Zhang, Y. Ou, Z. Fu, J. Ying, Y. Zong, B. Lang, C. Yang, Y. Zhou, X. Wang, H. Ji, Mn/CeO_2 contains enriched surface lewis acid sites and pore structures accelerated catalytic oxidation of propane at low temperature, Fuel, 2024, **378**, 132870.

58. L. Rodríguez-González, F. Hermes, M. Bertmer, E. Rodríguez-Castellón, A. Jiménez-López, U. Simon, The acid properties of H-ZSM-5 as studied by NH_3-TPD and 27Al-MAS-NMR spectroscopy, Appl. Catal. A: General, 2007, **328**, 174-182.

59. H. Zhang, J. Dong, Y. Li, F. Chen, R. Zhang, X. Xiang, R. Liu, J. He, S. Zhang, Synthesis of Tunable-Acidity Vanadium Phosphorus Oxide Catalysts Modified by Layered Double Oxide for the Selective Oxidation of n-Butane, Ind. Eng. Chem. Res., 2022, **61**, 3850-3859.

60. Y.-R. Liu, X. Li, W.-M. Liao, A.-P. Jia, Y.-J. Wang, M.-F. Luo, J.-Q. Lu, Highly Active Pt/BN Catalysts for Propane Combustion: The Roles of Support and Reactant-Induced Evolution of Active Sites, ACS Catal., 2019, **9**, 1472-1481.

61. W. Liu, S. Yang, H. Yu, S. Liu, H. Li, Z. Shen, Z. Song, X. Chen, X. Zhang, Boosting the total oxidation of toluene by regulating the reactivity of lattice oxygen species and the concentration of surface adsorbed oxygen, Sep. Purif. Technol., 2023,

View Article Online
DOI: 10.1039/D6EY00068A

325, 124597.

62. W. Zhu, X.-b. Wang, C. Li, X. Chen, W.-y. Li, Z. Liu, C. Liang, Defect engineering over Co_3O_4 catalyst for surface lattice oxygen activation and boosted propane total oxidation, J. Catal., 2022, **413**, 150-162.

63. L.-Y. Xu, C.-H. Wen, X.-H. Luo, W.-X. Zhang, X. Zhao, Q.-H. Yang, J.-Q. Lu, M.-F. Luo, J. Chen, Regulating the synergy of sulfate and Pt species in Pt/ZSM-5 for propane complete oxidation, Appl. Catal. B: Environ. Energy, 2024, **354**, 124135.

64. C. Feng, G. Xiong, C. Chen, Y. Lin, Z. Wang, Y. Lu, F. Liu, X. Li, Y. Liu, R. Zhang, Y. Pan. Highly dispersed Pt/Co_3O_4 catalyst constructed by vacancy defect inductive effect for enhanced catalytic propane total oxidation, Chinese J. Catal., 2025, **75**, 21-33.

65. C. Feng, Q. Gao, G. Xiong, Y. Chen, Y. Pan, Z. Fei, Y. Li, Y. Lu, C. Liu, Y. Liu. Defect engineering technique for the fabrication of $LaCoO_3$ perovskite catalyst via urea treatment for total oxidation of propane. Appl. Catal. B: Environ., 2022, **304**, 121005.

66. C. Feng, C. Chen, G. Xiong, D. Yang, Z. Wang, Y. Pan, Z. Fei, Y. Lu, Y. Liu, R. Zhang, X. L. Cr-doping regulates Mn_3O_4 spinel structure for efficient total oxidation of propane: Structural effects and reaction mechanism determination, App. Catal. B: Environ., 2023, **328**, 122528.

67. A. Tomita, T. Miki, Y. Tai, Effect of water treatment and Ce doping of Pt/Al_2O_3 catalysts on Pt sintering and propane oxidation, Res. Chem. Intermediat., 2021, **47**, 2935-2950.

68. L. Liu, W. Han, F. Dong, H. Feng, T. Zhicheng, Construction of framework

View Article Online
DOI: 10.1039/D6EY00068A

confined ordered mesoporous Pt/Ti_xAlO_y catalysts and applied for the catalytic oxidation of propane, Microporous Mesoporous Mat., 2022, **341**, 112111.

69. X. Gao, Y. Bai, H. Zhang, X. Wang, Catalytic Oxidation of n-Decane, n-Hexane, and Propane over Pt/CeO_2 Catalysts, ACS Omega, 2023, **8**, 6791-6800.

70. S. Viéitez-Calo, D.J. Morgan, S. Golunski, S.H. Taylor, M.V. Twigg, Structure Sensitivity and Hydration Effects in Pt/TiO_2 and Pt/TiO_2-SiO_2 Catalysts for NO and Propane Oxidation, Top. Catal., 2021, **64**, 955-964.

View Article Online
DOI: 10.1039/D6EY00068A

Table 1 Catalytic properties of $Pt/Ni_1Co_{0.5}AlO_x$ and its core-shell catalysts for propane oxidation.

Catalysts	dry			wet			difference	
	T_{50}[a] (°C)	T_{90}[a] (°C)	E_a[b] (kJ/mol)	T_{50}[a] (°C)	T_{90}[a] (°C)	E_a[b] (kJ/mol)	ΔT_{90}[c] (°C)	ΔE_a[c] (kJ/mol)
$Pt/Ni_1Co_{0.5}AlO_x$	317	374	41.6	376	450	51.0	76	9.4
$Pt/Ni_1Co_{0.5}AlO_x$@ZSM-5(5%)	353	440	49.4	354	420	48.4	-20	-1.0
$Ni_1Co_{0.5}AlO_x$@Pt/ZSM-5(3%)	293	368	39.7	332	393	44.3	25	4.6
$Ni_1Co_{0.5}AlO_x$@Pt/ZSM-5(5%)	323	400	44.8	313	410	46.0	10	1.2
$Ni_1Co_{0.5}AlO_x$@Pt/ZSM-5(10%)	336	450	50.6	340	455	53.0	5	2.4

[a] The reaction temperatures at 50% and 90% propane conversion under dry air and 5 vol% H_2O conditions.

[b] E_a values were obtained by calculating the slope of the Arrhenius curve for propane conversion under 20%.

[c] Difference between E_a and T_{90} of the same catalyst under dry air and 5 vol% H_2O conditions.

View Article Online
DOI: 10.1039/D6EY00068A

Table 2 Comparison of catalytic properties for propane oxidation of Pt-based catalysts reported in the literature with this work.

Catalysts	T_{50}[a] (°C)	T_{90}[a] (°C)	Pt content (wt%)	Concentration (ppm)	WHSV ($mL \cdot g^{-1} \cdot h^{-1}$)	Ref.
Pt/CeO_2	318	380	0.8	0.2% C_3H_8+2% O_2/Ar	150000	[7]
$1Pt/3.6Ce/Al_2O_3$-RWH	360	450	1.0	0.1% C_3H_8+10% O_2/Ar	40000	[67]
Pt/Al_2O_3	472	591	-	0.2% C_3H_8+5% O_2/Ar	30000	[68]
$Pt/Ti_{0.1}AlO_y$	416	529	-	0.2% C_3H_8+5% O_2/Ar	30000	[68]
Pt/CeO_2-SR	306	385	0.9	0.3% C_3H_8+20% O_2/N_2	30000	[69]
Pt/CeO_2-WI	334	389	1.0	0.3% C_3H_8+20% O_2/N_2	30000	[69]
1%Pt/TiO_2(bi-phasic)	355	400	1.0	0.5% C_3H_8+5% O_2/He	50000	[70]
$Pt/Ni_1Co_{0.5}AlO_x$	317	374	0.5	0.2% C_3H_8+5% O_2/Ar	30000	This work
$Pt/Ni_1Co_{0.5}AlO_x$@ ZSM-5(5%)	353	440	0.5	0.2% C_3H_8+5% O_2/Ar	30000	This work
$Ni_1Co_{0.5}AlO_x$@ Pt/ZSM-5(3%)	293	368	0.5	0.2% C_3H_8+5% O_2/Ar	30000	This work

[a] The reaction temperatures at 50% and 90% propane conversion under dry air conditions.

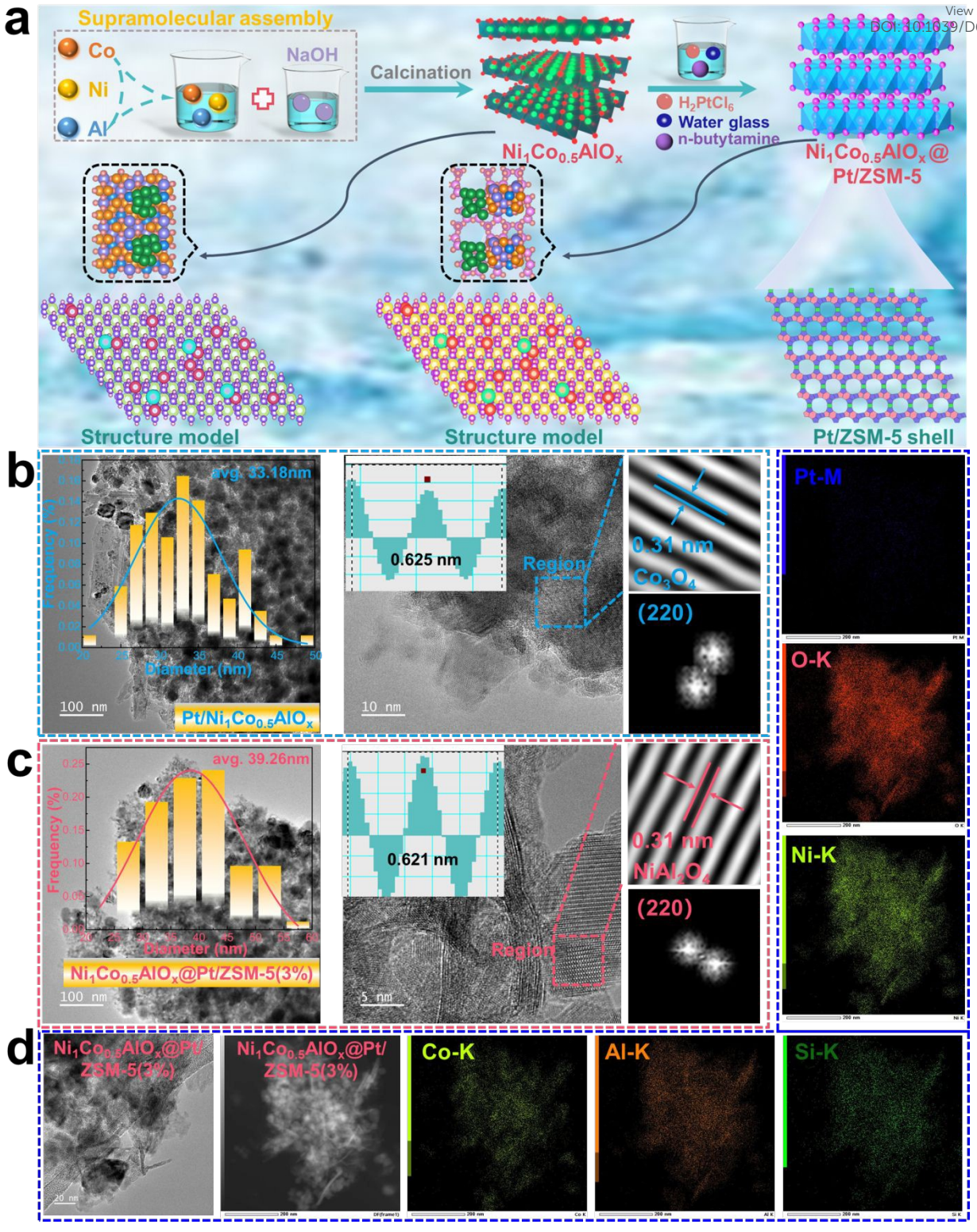

Fig. 1. (a) Schematic illustration of synthesis process for $Ni_1Co_{0.5}AlO_x$ and $Ni_1Co_{0.5}AlO_x$@Pt/ZSM-5 catalysts. TEM, HRTEM images and plane of $Pt/Ni_1Co_{0.5}AlO_x$ (b) and $Ni_1Co_{0.5}AlO_x$@Pt/ZSM-5(3%) (c) catalysts. TEM images and mapping analysis of $Ni_1Co_{0.5}AlO_x$@Pt/ZSM-5(3%) catalyst (d).

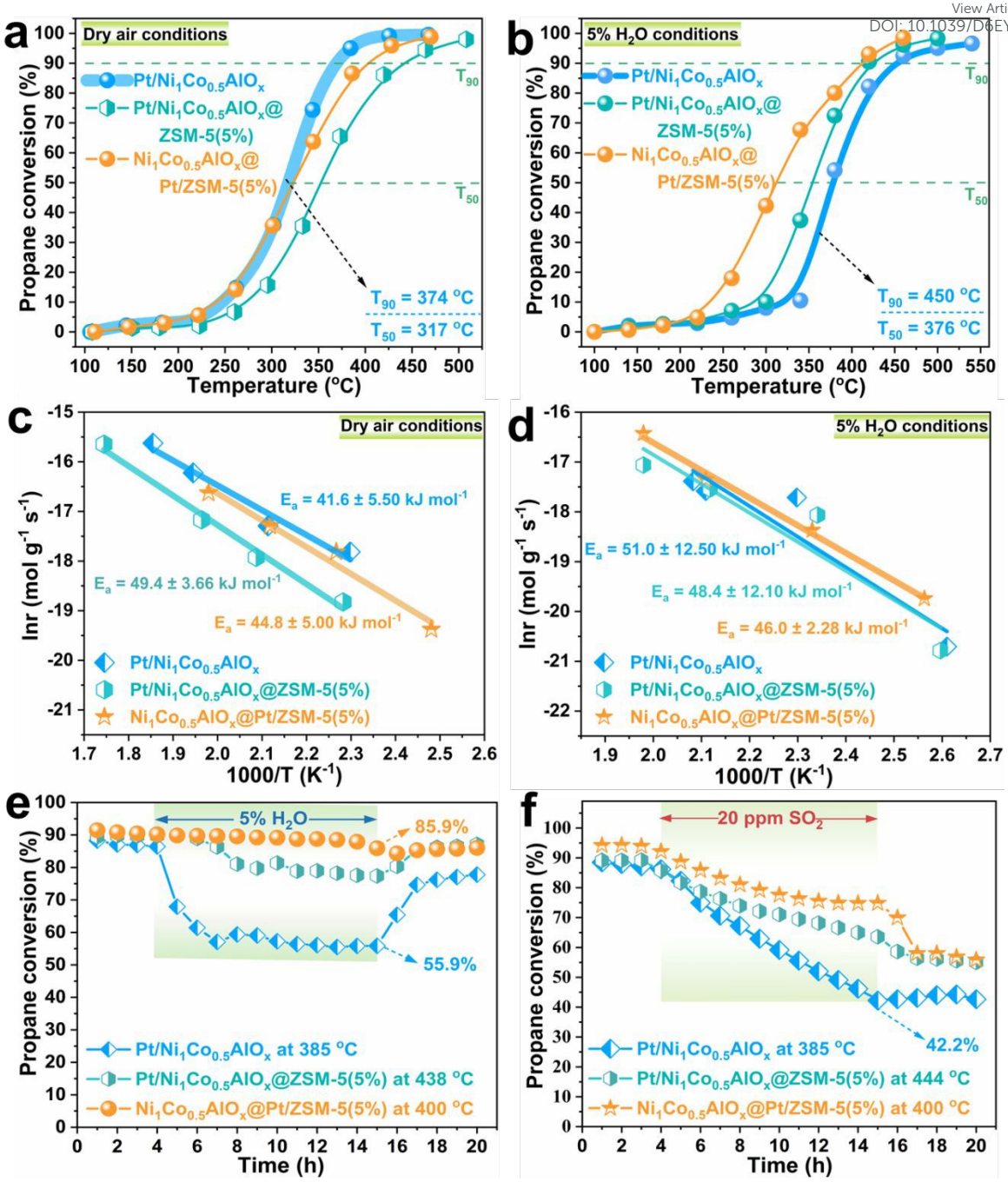

Fig. 2. Catalytic activity of $Pt/Ni_1Co_{0.5}AlO_x$ and its core-shell catalysts under dry air and 5 vol% H_2O conditions (a and b). E_a of $Pt/Ni_1Co_{0.5}AlO_x$ and its core-shell catalysts under dry air (c) and 5 vol% H_2O (d) conditions. Anti-H_2O ability (e) and Anti-SO_2 ability (f) of $Pt/Ni_1Co_{0.5}AlO_x$ and its core-shell catalyst.

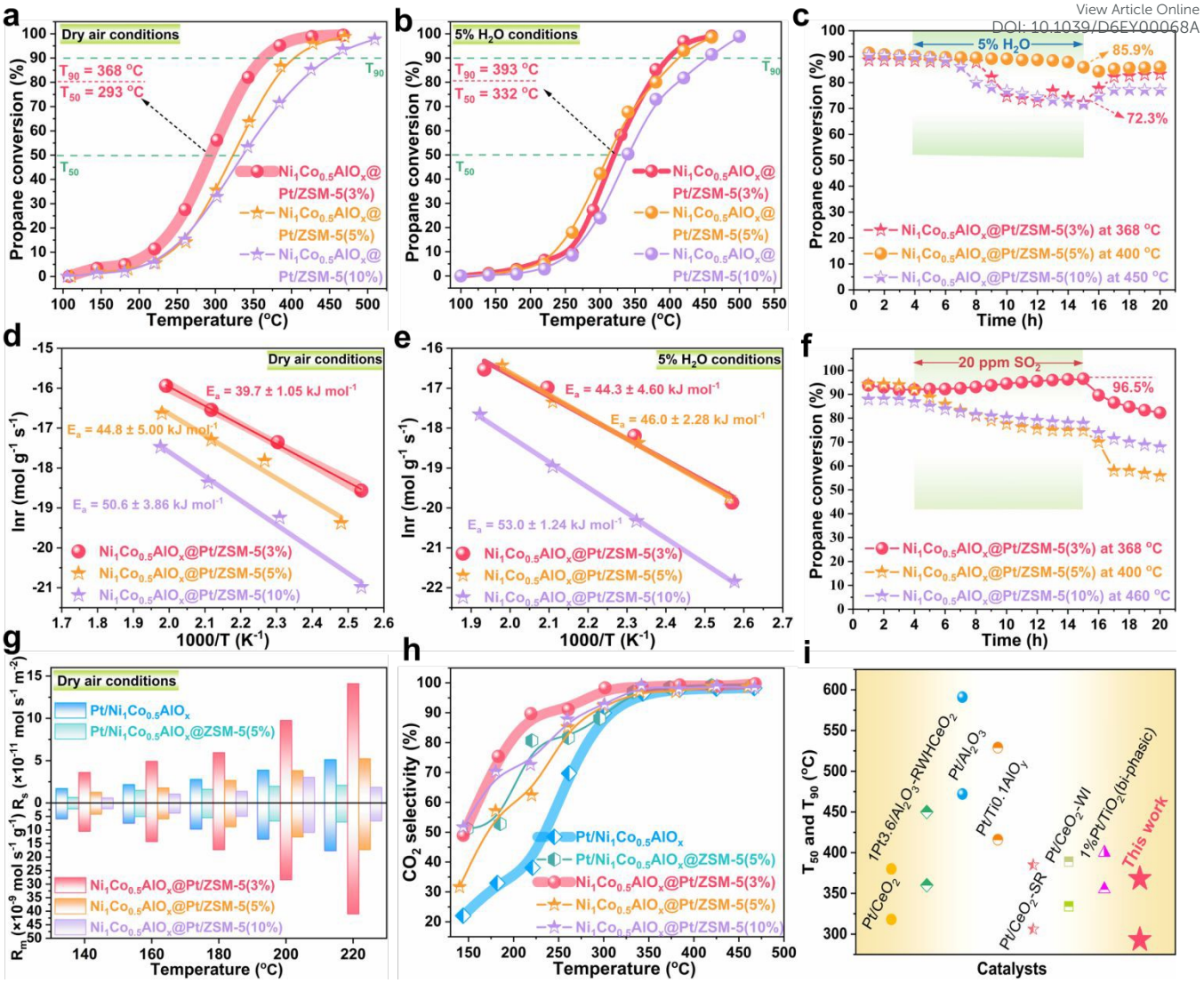

Fig. 3. Catalytic activity of core-shell structure $Ni_1Co_{0.5}AlO_x$@Pt/ZSM-5 catalyst under dry air and 5 vol% H_2O conditions (a and b). Anti-H_2O ability (c). E_a of core-shell structure $Ni_1Co_{0.5}AlO_x$@Pt/ZSM-5 catalyst under dry air (d) and 5 vol% H_2O (e) conditions. Comparison of R_s and R_m with respect to temperature variation (f). Anti-SO_2 ability (g) and CO_2 selectivity (h) of Pt/$Ni_1Co_{0.5}AlO_x$ and its core-shell catalyst. Comparison of catalytic properties for propane oxidation of Pt-based catalysts reported in the literature with this work (i).

View Article Online
DOI: 10.1039/D6EY00068A

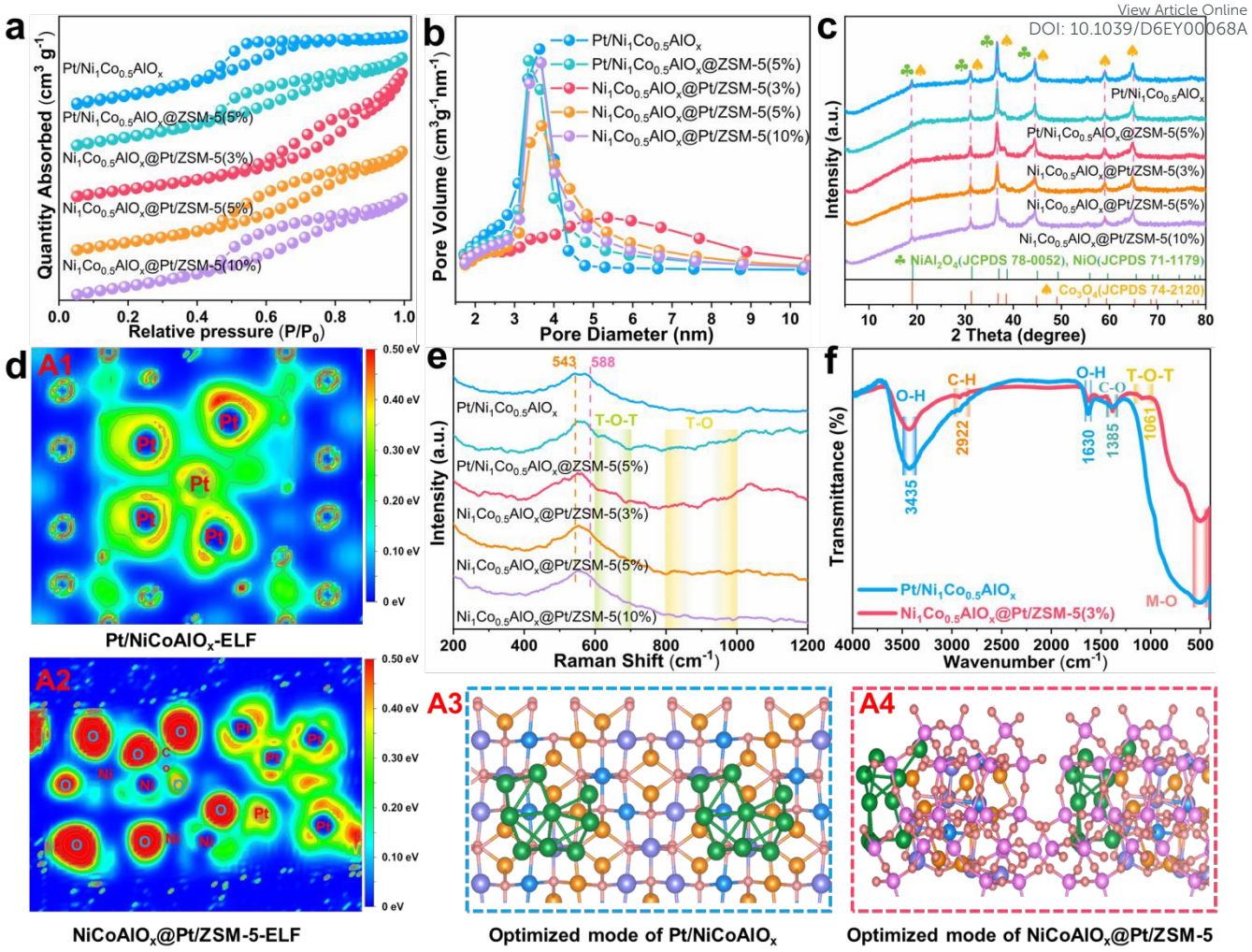

Fig. 4. Nitrogen adsorption-desorption isotherms (a), pore diameter distribution (b), and XRD (c) profiles of $Pt/Ni_1Co_{0.5}AlO_x$ and its core-shell catalysts. (d) The electron location function and optimized mode of $Pt/NiCoAlO_x$ and $Ni_1Co_{0.5}AlO_x$@Pt/ZSM-5. Raman (e), and FTIR (f) profiles of $Pt/Ni_1Co_{0.5}AlO_x$ and its core-shell catalysts.

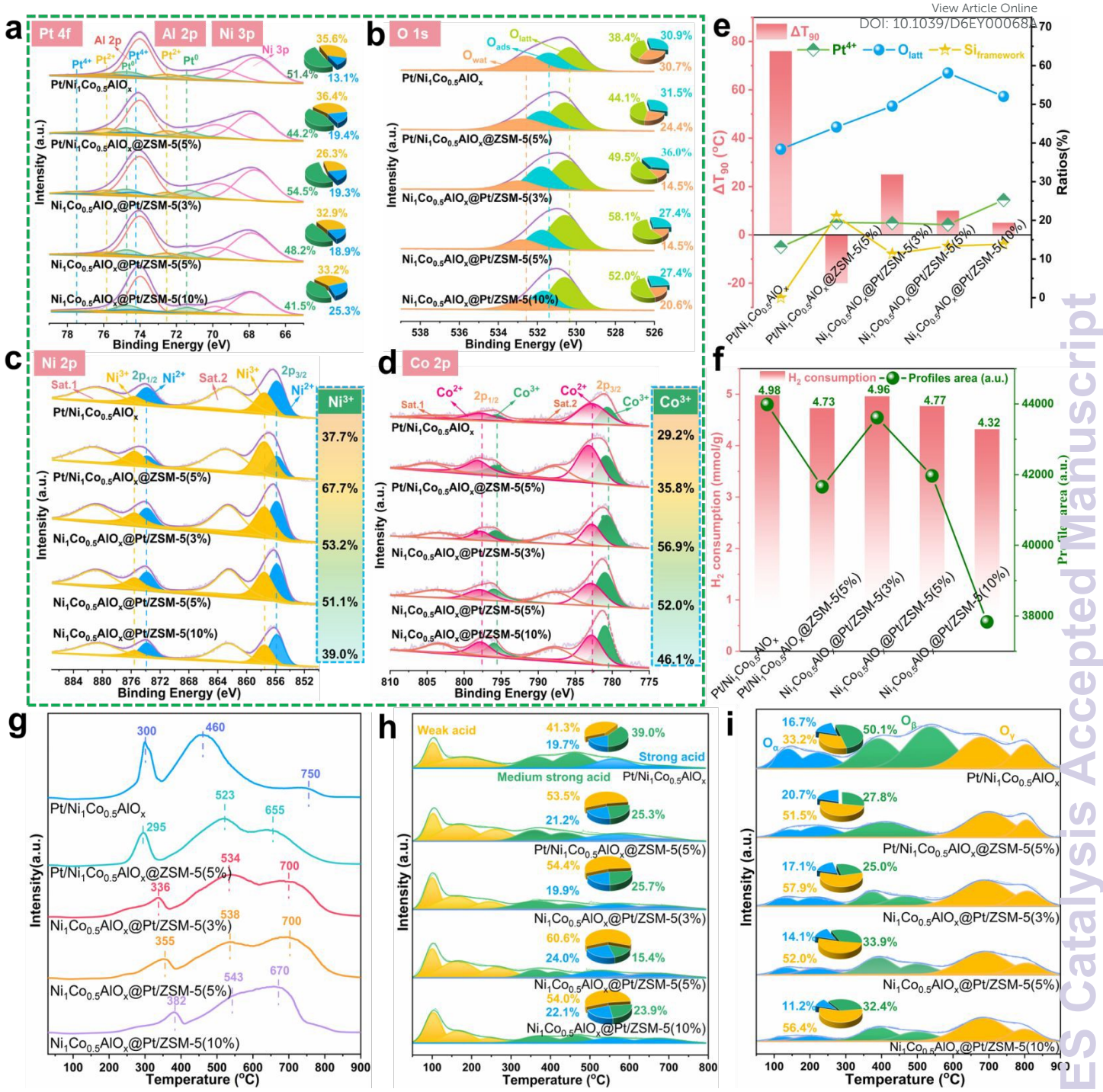

Fig. 5. XPS spectra of Pt 4f, Al 2p and Ni 3p (a), O 1 s (b), Ni 2p (c) and Co 2p (d) on $Pt/Ni_1Co_{0.5}AlO_x$ and its core-shell catalysts. Ratios of Pt^{4+}/Pt_{total}, O_{latt}/O_{total}, $Si_{framework}/Si_{total}$ versus ΔT_{90} (e) of $Pt/Ni_1Co_{0.5}AlO_x$ and its core-shell catalysts. H_2 consumption (f), H_2-TPR profiles (g), NH_3-TPD (h) and O_2-TPD (i) profiles of $Pt/Ni_1Co_{0.5}AlO_x$ and its core-shell catalysts.

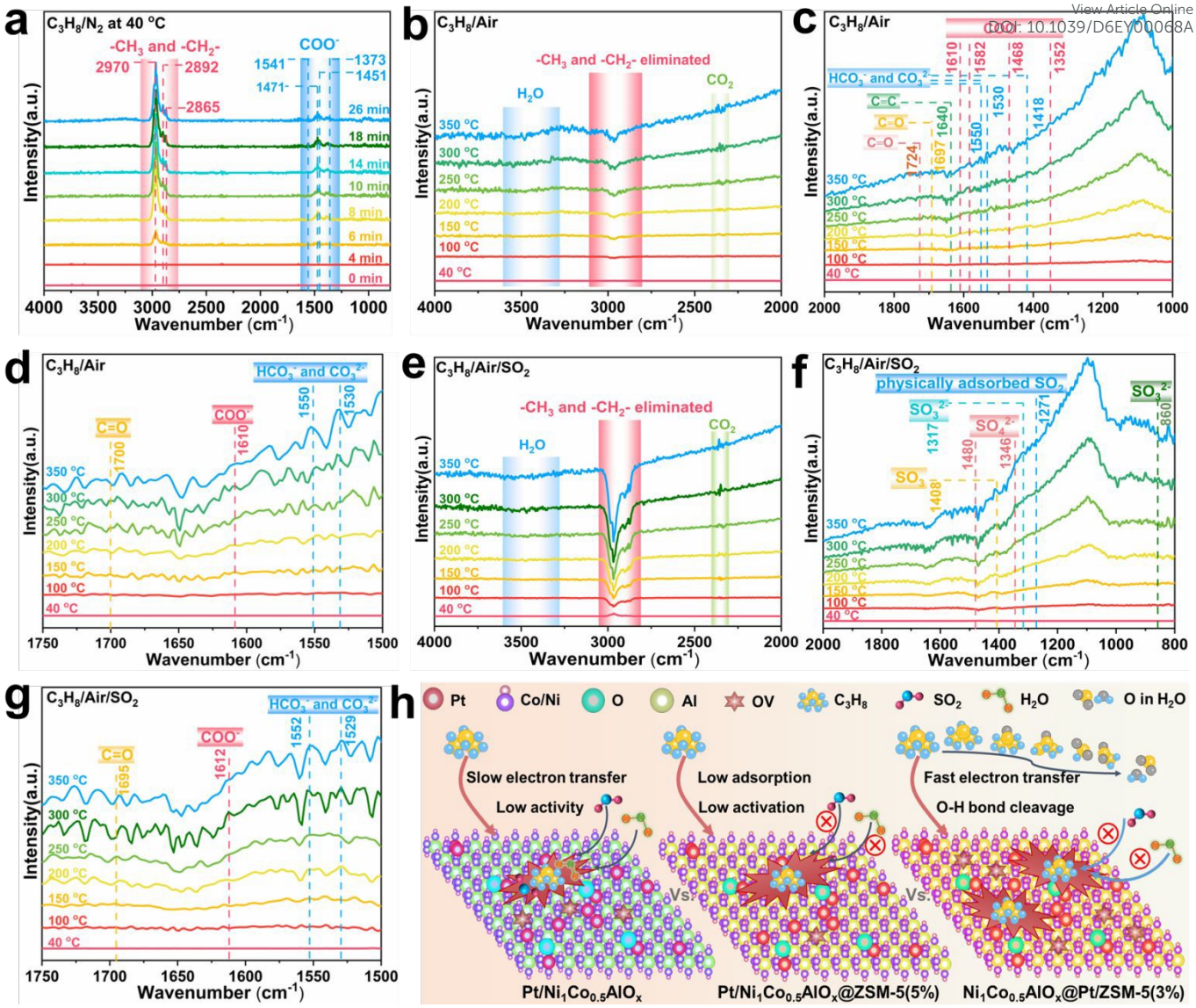

Fig. 6. In-situ DRIFTS spectra on the $Ni_1Co_{0.5}AlO_x$@Pt/ZSM-5(3%) catalyst: Propane adsorption at 40 °C (a), propane oxidation at air (b, c, d) and propane oxidation at air/SO_2 (e, f, g). Schematic illustration of H_2O/SO_2-tolerant propane oxidation mechanism over $Ni_1Co_{0.5}AlO_x$@Pt/ZSM-5(3%) catalyst (i).

View Article Online
DOI: 10.1039/D6EY00068A

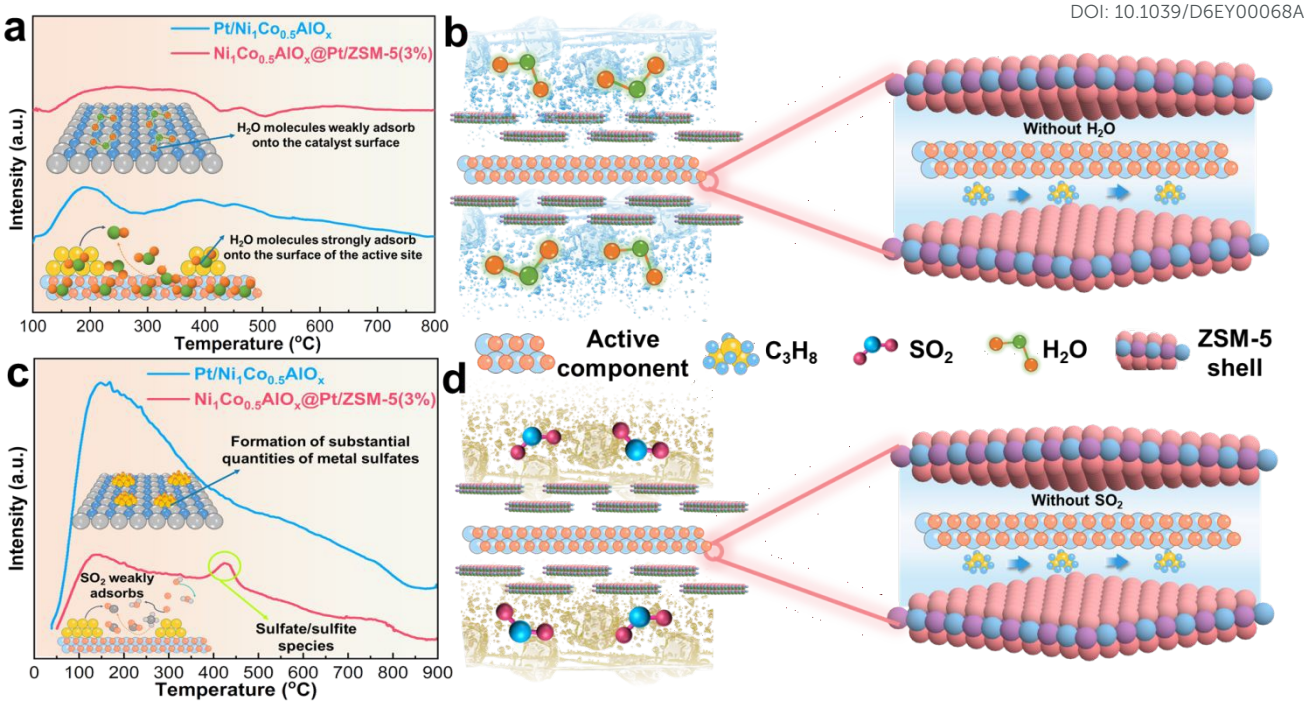

Fig. 7. H_2O-TPD profiles (a) of $Pt/Ni_1Co_{0.5}AlO_x$ and $Ni_1Co_{0.5}AlO_x$@Pt/ZSM-5(3%) catalysts. The schematic diagram of ZSM-5 shell water resistance mechanism (b). SO_2-TPD profiles of $Pt/Ni_1Co_{0.5}AlO_x$ and $Ni_1Co_{0.5}AlO_x$@Pt/ZSM-5(3%) catalysts (c). The schematic comparison showing how the ZSM-5 shell protects the active component from SO_2 poisoning (d).

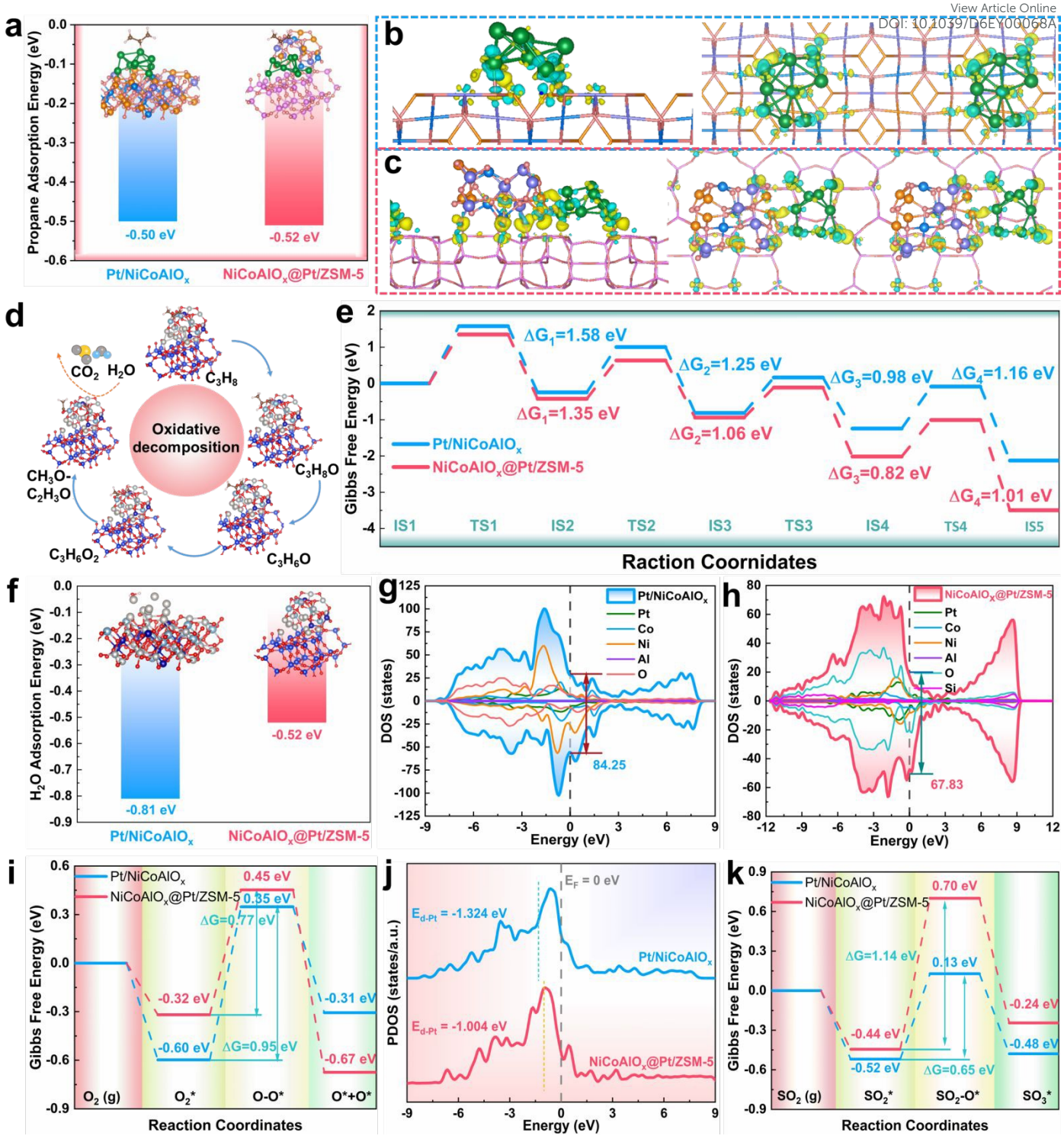

Fig. 8. The adsorption calculations of propane (a) on Pt/NiCoAlO$_x$ and NiCoAlO$_x$@Pt/ZSM-5 model surfaces. Charge density difference plot for (b) Pt/NiCoAlO$_x$ and (c) NiCoAlO$_x$@Pt/ZSM-5. The isosurface value is 0.01 e·Bohr^{-3}. Yellow is positive and blue is negative. The oxidative decomposition pathway of

View Article Online
DOI: 10.1039/D6EY00068A

propane on the $NiCoAlO_x$@Pt/ZSM-5 (d). Primitive steps and Gibbs free energy diagram of propane oxidation over the Pt/$NiCoAlO_x$ and $NiCoAlO_x$@Pt/ZSM-5 (e). The adsorption calculations of H_2O (f), density of state (g and h), the adsorption and dissociation calculations of O_2 (i), Projected DOS (j) and the calculation of SO_2 adsorption (k) on Pt/$NiCoAlO_x$ and $NiCoAlO_x$@Pt/ZSM-5 model surfaces.

View Article Online
DOI: 10.1039/D6EY00068A

Data availability

The data that support the findings of this study are available in the supporting information of this article. Supporting information including the results from TEM, HRTEM, catalytic activity, reaction kinetics calculations, XRD, BET, H_2-TPR, O_2-TPD, NH_3-TPD, in-situ DRIFTS and DFT calculations.